Thermodynamics of Active Matter: Tracking Dissipation across Scales

Robin Bebon,[1] Joshua F. Robinson,[2,3] and Thomas Speck[1,*]

[1]*Institute for Theoretical Physics IV, University of Stuttgart, Heisenbergstrasse 3, 70569 Stuttgart, Germany*

[2]*Institut für Physik, Johannes Gutenberg-Universität Mainz, Staudingerweg 7-9, 55128 Mainz, Germany*

[3]*H. H. Wills Physics Laboratory, University of Bristol, Bristol BS8 1TL, United Kingdom*

(Received 22 December 2023; revised 24 June 2024; accepted 1 April 2025; published 12 May 2025)

The concept of entropy has been pivotal in the formulation of thermodynamics. For systems driven away from thermal equilibrium, a comparable role is played by entropy production and dissipation. Here, we provide a comprehensive picture of how local dissipation due to effective chemical events manifests on large scales in active matter. We start from a microscopic model for a single catalytic particle involving explicit solute molecules and show that it undergoes directed motion. Leveraging stochastic thermodynamics, we calculate the average entropy production rate for interacting particles. We then show how the model of active Brownian particles emerges in a certain limit, and we determine the entropy production rate on the level of the hydrodynamic equations. Our results augment the model of active Brownian particles with rigorous expressions for the dissipation that cannot be inferred from their equations of motion, and we illustrate consequences for wall aggregation and motility-induced phase separation. Notably, our bottom-up approach agrees with the "naive" result from Onsager's principle for the local dissipation rate.

DOI: 10.1103/PhysRevX.15.021050 Subject Areas: Soft Matter, Statistical Physics

I. INTRODUCTION

The development of macroscopic thermodynamics has in no small part been driven by the industrial revolution and its need for engines that exploit the transformation of heat into usable work [1]. A crucial step had been to recognize *entropy* as the central constraint limiting the amount of extractable work. With the rapidly increasing capacity to image and manipulate systems on the micro- and even nanoscale, the scope of thermodynamics and statistical mechanics has vastly expanded. *Entropy production* has since emerged as an important benchmark to characterize systems that are steadily driven away from thermal equilibrium [2–6]. In particular, living matter in the form of bacteria and cells must convert chemical energy to organize themselves and their environments in space and time and to provide essential functions such as sensing and signaling [7–9], replication [10–12], and locomotion [13–15].

Basic features of living matter, such as locomotion, can also be realized in synthetic systems by harnessing a wide range of physical mechanisms that are studied within the field of (motile) active matter [16–18]. Experimental realizations now routinely exploit diffusiophoresis [19,20], thermophoresis [21], photoactivation [22,23], Quincke rotation [24,25], electrophoresis [26], and acoustophoresis [27] to realize persistent yet autonomous motion of individual agents. Irrespective of the exact microscopic details, any directed motion is necessarily accompanied by local time-reversal symmetry breaking and causes the continual dissipation of either residual or chemical free energy. While (motile) active matter undoubtedly falls into the realm of nonequilibrium systems, the majority of theoretical approaches remain founded in local equilibrium assumptions such as the determination of the self-propulsion speed from approximate solutions of the Stokes equation [28–40].

On a coarser (mesoscopic) scale, minimal models capture the persistent motion of active particles through a self-propulsion term directed along an orientation that undergoes rotational diffusion—so-called active Brownian particles (ABPs) [17,18]. Suspensions of interacting motile particles have undergone substantial exploration. Of particular interest is the spontaneous aggregation of dense (liquid) domains surrounded by a dilute (gaseous) background even in the absence of cohesive forces, which is known as motility-induced phase separation (MIPS) [20,22,41–47]. The goal of quantifying collective behavior led to macroscopic field theories. Their derivation typically follows one of two routes: Top-down approaches infer the phenomenological equations of motion from conservation laws and symmetries [16,48–50], whereas bottom-up

*Contact author: thomas.speck@itp4.uni-stuttgart.de

approaches systematically coarse-grain the microscopic degrees of freedom into hydrodynamic fields and their evolution equations [51–57]. While top-down approaches enjoy great popularity due to their accessibility by virtue of an intuitive construction scheme, systematic bottom-up approaches have the advantage that they establish a connection between effective parameters of the field theory and parameters of the underlying microscopic model. Such a deeper understanding is crucial for the design of new material properties through tuning microscopic parameters.

Close to equilibrium in the (local) linear response regime, the framework of linear irreversible thermodynamics [58] can be used to derive equations of motion for coarse-grained degrees of freedom without explicit knowledge of the underlying microscopic dynamics. This approach dates back to the seminal work of Onsager [59,60] and has a long history in the modeling of complex soft materials [61] such as liquid crystals under shear flow [62] and chemically driven biomolecular motors [63]. Most importantly, transport properties due to small perturbations, such as thermal gradients and electrical fields, are encoded in equilibrium correlation functions. By postulating a linear coupling between the thermodynamic driving forces (commonly referred to as *affinities*) and their conjugate macroscopic currents, irreversible thermodynamics provides a systematic route to the dissipation of near-equilibrium dynamics [58] and the derivation of thermodynamically consistent evolution equations.

Going beyond linear response, stochastic thermodynamics [64–67] has emerged as a comprehensive framework to treat systems dominated by fluctuations. In its essence, it methodically extends (typically macroscopic) thermodynamic notions to individual fluctuating trajectories of small (e.g., molecular-sized [68–70]) systems. Stochastic thermodynamics provides, as one of its hallmarks, fundamental connections between equilibrium and nonequilibrium quantities through the celebrated fluctuation relations [71–75]. A second hallmark is the equality of dissipated heat, as inferred from the stochastic first law, with the behavior of path probabilities under time reversal entering the second law of thermodynamics. More recent endeavors have focused on expanding the tool set of thermodynamic inference [76], where consistency constraints are enforced to derive experimentally accessible estimators of the entropy production which is notoriously hard to measure. Prominent examples include the thermodynamic uncertainty relation [77–79], its numerous generalizations [80–85], and novel approaches involving the waiting time statistics of partially observable (semi-)Markov models [86–90]. Additionally, connections to macroscopic theories, where fluctuations play a subordinate role [91–93], and systems with spatially extended correlations [56,94–97] are currently under scrutiny.

The framework of stochastic thermodynamics has found application in various attempts at quantifying the nonequilibrium character of active matter [98–104]. To this end, a quantity that attracted immense interest, from both a theoretical [105–114] and experimental [115–117] perspective, is the irreversibility encoded in the time evolution of *observable* degrees of freedom, also referred to as "informatic" or path entropy production [109,111,113,118].

Only when including *all* degrees of freedom that contribute to dissipation does the path entropy production equal the *thermodynamic* entropy production, which, in turn, relates to dissipation. Indeed, the standard recipes of stochastic thermodynamics applied to minimal active matter models [99,103,105,106,108–111,119–124] lead to inconsistencies that have greatly obscured the correct identification of the dissipated heat. While an accurate thermodynamic theory for active matter is necessary to study energy balances in living matter [125,126] and to design efficient active (heat) engines [127–136], so far few attempts have been made at formulating thermodynamically consistent models of active agents [137–145].

The need for a thermodynamically consistent foundation becomes even more apparent at the level of field theories, which are, by construction, ignorant of microscopic details required for determining dissipation. At least close to equilibrium, it is thus tempting to conjecture the validity of linear irreversible thermodynamics in the presence of local drives that are characteristic for active matter [146]. In theory, treating the locally supplied free energy as a small perturbation away from Boltzmann equilibrium paves the way to a linear thermodynamics, yielding expressions for the dissipation of active matter on different scales. While it has proven successful in the study of phoretically propelled Janus particles [147], shown to reproduce the behavior of the cell cytoskeleton for hydrodynamic theories of active gels [148–150], and applied to a broad class of active field theories [146], its universal applicability, nonetheless, remains an open question.

Although coarse-graining necessarily sacrifices some information, carefully tracking the *thermodynamically relevant* degrees of freedom during the coarse-graining procedure may allow a more rigorous underpinning of the thermodynamics of active field theories. Here, we present and implement a bottom-up approach (cf. Fig. 1) that starts from an explicit model involving molecular solutes (Sec. II). The interconversion of these solutes at the surface of colloidal particles is shown to lead to self-propulsion, for which solute flux and force on the colloidal particle can be explicitly calculated. We then introduce an effective model, in which tight coupling between fuel consumption and directed displacement reproduces the explicit model. In Sec. III, we track its dissipation through several coarse-graining steps: First, integrating out the solute molecules and expanding in a small parameter yields the evolution equation of interacting active Brownian particles together with exact expressions for the dissipation caused by each active particle. The calculated dissipation rate shows that active particle propulsion is accompanied by a constant

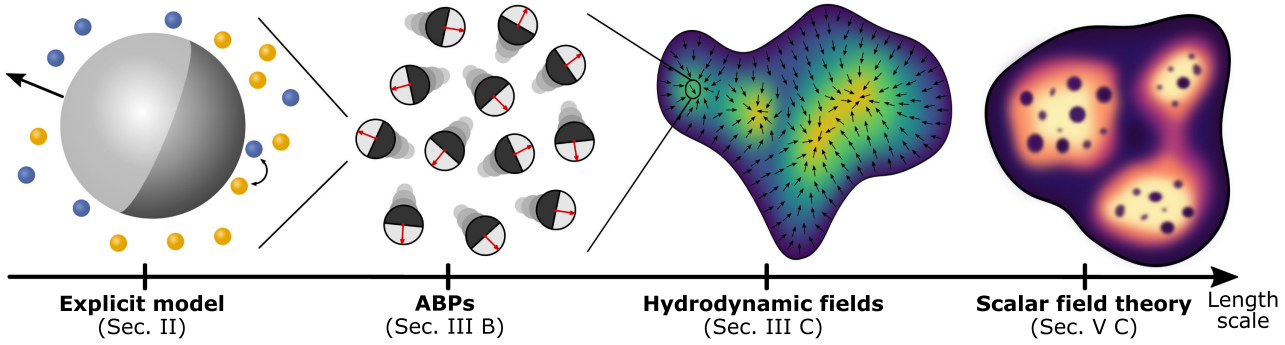

FIG. 1. Schematic depiction of the studied length scales. Starting in Sec. II, we consider a single catalytic particle with explicit fuel molecules. In Sec. III B, we establish a connection between this explicit model and a thermodynamically consistent derivation leading to the model of active Brownian particles (ABPs). We then turn to a macroscopic description in the form of effective hydrodynamic fields in Sec. III C. Lastly, we eliminate the polarization field in Sec. V C, leaving us with a scalar field theory for the density alone.

solute flux between substrate and product reservoirs providing the work necessary to maintain directed motion. Second, going from particle-based to hydrodynamic fields yields as our central result an *exact* expression for the dissipated heat, both local and averaged, in terms of the density and polarization fields.

Building on these results, we discuss applications and ramifications in Secs. IV and V. First, we apply our results to illustrative examples that unveil the nontrivial thermodynamic footprint of confinement (Sec. IV A) and the dissipation field of an active suspension undergoing MIPS (Sec. IV B). Second, we explore the limit of small driving affinity—the linear response regime—and show how our results can be cast into a form that is consistent with the phenomenological framework of linear irreversible thermodynamics (Sec. V B). We pay particular attention to an apparent "gauge freedom" and how to resolve it. Lastly, we sketch a possible strategy to extend our results to scalar field theories (Sec. V C).

II. THE EXPLICIT MODEL: A SINGLE PARTICLE WITH FUEL MOLECULES

A. Definition of model

Our starting point is a single spherical colloidal particle submerged in an isothermal solvent at temperature T. For convenience, we define the inverse thermal energy $\beta \equiv (k_B T)^{-1}$. The solvent is treated as an effective medium that gives rise to stochastic forces, the strength of which $D_0 = \mu_0 k_B T$ is determined by the particle mobility μ_0. The colloidal particle interacts with uncharged and much smaller (molecular) solutes, which we distinguish as either substrate (S) or product (P). For simplicity, we assume that both solute species have the same diffusion coefficient D but interact through different isotropic potentials $u_\alpha(r)$ with the colloidal particle, where α is either S or P. Both potentials have a finite range $r < r_C$ beyond which the solutes diffuse freely. The surface of the colloidal particle is divided into inert and chemically active regions. Only within these active regions is the conversion between substrate and product possible due to a catalytic lowering of the activation barrier. Here, we consider geometries with rotational symmetry defining the orientation $\mathbf{e}$, the simplest example for which is a Janus particle with two distinct hemispheres as depicted in Fig. 2(a).

In the following, we choose the center of the colloidal particle as the origin so that $\mathbf{r}$ denotes the position of a solute, $r = |\mathbf{r}|$ is its distance from the origin, and θ is the polar angle with the orientation $\mathbf{e}$. The conversion between substrate and product is a stochastic process described by two rates, k^+ for $S \to P$ and k^- for $P \to S$. Both rates are zero except within the catalytic zone, where they obey the detailed balance condition

$$\frac{k^+(r,\theta)}{k^-(r,\theta)} = e^{-\beta[u_P(r)-u_S(r)]} \equiv e^{-\beta\Delta u(r)}, \tag{1}$$

guaranteeing that the composite system will eventually reach thermal equilibrium. The equilibrium state has equal numbers of substrate and product solutes, as we neglect any energy states internal to the reactants. Coupling to external reservoirs introduces a solute flux that drives the colloidal particle due to a nonuniform distribution of solute molecules.

Our model differs from the prevalent approach to model motility of catalytic Janus particles [29,30,33,35,40,151], which is through the hydrodynamic boundary layer approximation: The colloid is imagined to exert a force on nearby solute molecules, which propagates as a force density to the surrounding solvent [28]. In this conventional approach, nonuniform current boundary conditions are then enforced at the particle surface, leading to inhomogeneous concentration profiles (and, thus, gradients) that determine the self-propulsion speed. Such an independent treatment of surface potential and boundary conditions, however, violates local detailed balance, and solvent flow cannot be driven by local concentration gradients alone [152]. Here, we present an alternative model without explicit solvent

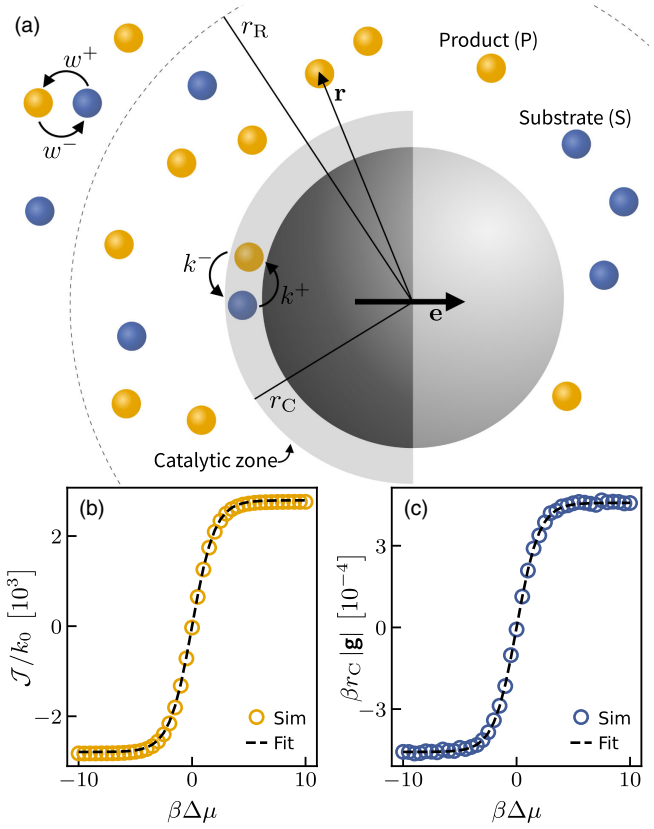

FIG. 2. (a) Sketch of a colloidal Janus particle moving in the presence of two molecular solutes: substrate (blue) and product (yellow). One of the hemispheres is chemically inert and the other active (shaded zone), within which substrate can be converted into product and vice versa. In simulations, we implement a chemostat through a reservoir region for $r > r_R$, wherein interconversion occurs with rates $\omega^{\pm}$. (b),(c) Results of Brownian dynamics simulations involving a single stationary catalyst centered around the origin and 32×10^5 ideal reactants. Shown are (b) the chemical flux $\mathcal{J}$ and (c) the force magnitude $|\mathbf{g}|$ on a single catalytic particle as a function of the chemical potential difference, verifying Eqs. (3) and (2). Fitting our theoretical results, we obtain $k_{\text{eff}} \approx 1396 k_0$ from (b) and $\lambda \approx 1.6 \times 10^{-7} r_C$ from (c).

flows whereby particle-solute interactions are described via explicit pair potentials. This allows for an analytical solution—without introducing a slip velocity—and guarantees the correct stochastic energetics of the chemically driven system.

B. Directed motion

We now show that this model of explicit solute molecules exhibits directed motion. To this end, we consider an ideal chemostat that maintains constant densities $\bar{c}_\alpha$ far away from the colloidal particle ($r \to \infty$) with chemical potential difference $\Delta\mu \equiv \mu_S - \mu_P = k_B T \ln(\bar{c}_S/\bar{c}_P)$. The chemostat induces a flux of solutes from substrate to product reservoir, which performs work on the colloidal particle. The resulting speed is determined by the force due to the imbalance of solute concentrations on the different regions.

In Appendix A, we calculate the solute densities around the colloidal particle within a thin interaction layer approximation; i.e., solutes interact with the colloidal particle only within a spherical shell of effective thickness ℓ that is much smaller than the particle diameter. From these solute densities, we extract the functional form of the total force:

$$\mathbf{g} = \frac{\ell k_0}{\beta D} h_1 \bar{c} \mathcal{V} \tanh\left(\frac{\beta\Delta\mu}{2}\right) \hat{\mathbf{e}}_z \tag{2}$$

acting on the colloidal particle with the total solute concentration $\bar{c} = \bar{c}_S + \bar{c}_P$. Here, $\mathcal{V}$ is akin to an effective volume [defined in Eq. (A14)] independent of the chemostat, and h_1 is a geometric coefficient quantifying the asymmetry between active and inert regions [defined in Eq. (A6)]. Furthermore, we obtain the average net flux

$$\mathcal{J} = 2k_{\text{eff}} \tanh\left(\frac{\beta\Delta\mu}{2}\right) \tag{3}$$

of solute particles from the substrate to product reservoir. Both of these quantities vanish in equilibrium where $\Delta\mu = 0$ and $\bar{c}_S = \bar{c}_P = \bar{c}_{\text{eq}}$. The flux depends on the effective attempt rate

$$k_{\text{eff}} \equiv 2\pi\bar{c} \int_{|\boldsymbol{\xi}|<r_C} \mathrm{d}\boldsymbol{\xi}\, \xi^2 k^-(\xi,\theta) e^{-\beta u_P(\xi)}. \tag{4}$$

The average propulsion speed $v_0 = \mu_0|\mathbf{g}| = \lambda\mathcal{J}$ along the orientation associated with the chemically induced displacements can, thus, be written as the flux (number of events per time) times an effective jump length:

$$\lambda \equiv \frac{1}{2}\frac{D_0}{D}\frac{k_0}{k_{\text{eff}}} h_1 \bar{c} \mathcal{V} \ell. \tag{5}$$

Each conversion thereby "pushes" the particle an effective distance λ along its orientation.

C. Simulations

We verify Eq. (2) for the force and Eq. (3) for the flux by performing Brownian dynamics simulations in a finite volume V with periodic boundaries. The box contains 32×10^5 noninteracting solutes. A single stationary colloid at the center of the box is represented by the external potentials $u_S(r)$ and $u_P(r)$. These potentials are short-ranged and repulsive, with interactions occurring only for distances $r < r_C$ (for details, see Appendix F 1).

We introduce a reservoir region $r > r_R$ [see Fig. 2(a)], wherein conversions take place with constant rates

$$\frac{w^+}{w^-} = K e^{\beta\Delta\mu} = K\frac{\bar{c}_S}{\bar{c}_P} \tag{6}$$

obeying *local* detailed balance [66,153,154]. The constant K appearing here corrects for the finite box volume, which shifts the equilibrium chemical potential due to the presence of the catalyst ($K \to 1$ as $V \to \infty$) and is given in Appendix F 1.

Within the catalytic zone $r < r_C$, we allow for conversions with rates

$$k^{\pm}(r,\theta) = k_0 h(\theta)\left[1 + e^{\pm\beta\Delta u(r)}\right]^{-1} \tag{7}$$

that obey the detailed balance condition Eq. (1). Here, k_0 is an attempt rate, and $h(\theta)$ is an indicator function that is unity on active and zero on inert regions. We perform simulations with chemical potentials $\beta\Delta\mu \in [-10, 10]$ and calculate the solute flux [Fig. 2(b)] together with the total force [Fig. 2(c)]. Fitting the analytical expression for the solute flux [Eq. (3)] for k_{eff}, we find, in excellent agreement with simulation data, $k_{\text{eff}} \approx 1396 k_0$ as the effective attempt rate. Plugging this into the expression for the force [Eq. (2)], we further obtain $\lambda \approx 1.6 \times 10^{-7} r_C$ by fitting the simulated forces. With r_C comparable to the radius of a colloidal particle (i.e., hundreds of nanometers to a few microns), the obtained displacement length is of the order of approximately 0.01 to 0.1 pm, in reasonable agreement with previous studies based on boundary layer approaches for phoretically propelled particles [29,32,155]. Moreover, since k_{eff} implicitly depends of the interaction layer thickness ℓ due to the limited support of the integral in Eq. (4), we recover the commonly reported $v_0 \propto \lambda k_{\text{eff}} \sim \ell^2$ scaling of the self-propulsion speed [29,32,152,155].

III. TRACKING DISSIPATION

A. Effective chemical events

The central lesson of the previous section (Sec. II) has been that we can map the explicit model onto effective chemical events with attempt rate k_{eff}. While such an effective model has been proposed earlier [139], we have shown here that it follows naturally from a more microscopic description involving the conversion of fuel molecules. In the effective model, we assume that chemical reactions between solute and product molecules are catalyzed on the colloidal surface. Free energy $\Delta\mu$ is either liberated ($S \to P$) or consumed ($P \to S$) depending on the direction. Moreover, each reaction coincides with a displacement of small but finite length λ, which is known as *tight coupling* [135,138,139,156]. While we have obtained an explicit expression [Eq. (5)], in the following, we treat λ as a parameter of the effective model. Clearly, the chemical events are stochastic in nature, allowing us to model their dynamics as an effective two-state model where transitions occur with rates κ^+ in the forward and κ^- in the backward direction (see Fig. 3). The detailed balance condition [Eq. (1)] is then replaced by

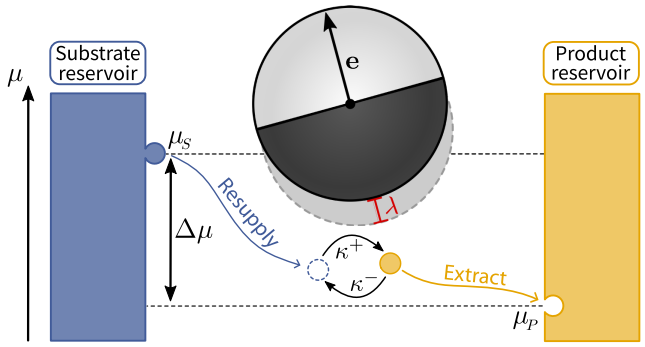

FIG. 3. Schematic illustration of a free catalytic particle undergoing effective chemical events. After each chemical event, converting substrate into product, the particle is displaced by a small distance λ along its orientation $\mathbf{e}$. To assure ideal substrate and product concentrations, external chemostats instantly resupply or remove the used and produced reaction constituents from or to (infinite) reservoirs. If the backward reaction takes place instead, this routine is reversed, and the particle is displaced against its orientation.

$$\frac{\kappa^+}{\kappa^-} = e^{\beta\Delta\mu}, \tag{8}$$

assuming that the reservoirs of solute and product molecules are ideal in the sense that concentrations, and, thus, the driving affinity $\Delta\mu$, remain constant at all times.

The evolution equation for the probability $\psi(\mathbf{r}, t)$ of the particle position $\mathbf{r}$ reads

$$\frac{\partial\psi}{\partial t} = -\nabla\cdot(v_0\mathbf{e}\psi) + D^c\nabla^2\psi \tag{9}$$

in the limit $\lambda \to 0$ of vanishing displacement. Here,

$$v_0 \equiv \lambda(\kappa^+ - \kappa^-) = 2k_{\text{eff}}\lambda\tanh\left(\frac{\beta\Delta\mu}{2}\right) \tag{10}$$

is the self-propulsion speed, where in the second step we assume symmetric rates

$$\kappa^+ = 2k_{\text{eff}}\frac{\bar{c}_S}{\bar{c}}, \qquad \kappa^- = 2k_{\text{eff}}\frac{\bar{c}_P}{\bar{c}} \tag{11}$$

obeying Eq. (8). This speed agrees exactly with the result obtained for the explicit model. At quadratic order in λ, the chemical events alone induce translational diffusion with coefficient

$$D^c \equiv \frac{\lambda^2}{2}(\kappa^+ + \kappa^-) = k_{\text{eff}}\lambda^2, \tag{12}$$

which has no dependence on $\Delta\mu$ and scales as $D^c \propto \bar{c}$ [cf. Eq. (4)].

B. The mesoscale: Active Brownian particles

1. A thermodynamically consistent many-body model

We now extend the model of effective chemical events to N interacting active particles. The full state of the system is described by the position $\mathbf{r}_i$ and orientation $\mathbf{e}_i$ of each particle $i \in \{1, \ldots, N\}$ together with the net number n_i of chemical events. Each active particle is subjected to three stochastic processes. The first process governs positional changes leading to particle currents:

$$\mathbf{j}_i^{\mathrm{p}} \equiv \mu_0(\mathbf{F}_i^{\mathrm{ex}} - \nabla_i U)\Psi - D_0 \nabla_i \Psi \tag{13}$$

due to translational diffusion as well as interparticle and external forces. The potential energy $U(\mathbf{r}^N) \equiv \sum_{i<j} u(|\mathbf{r}_i - \mathbf{r}_j|)$ is composed of pair interactions with (colloidal) pair potential $u(r)$, and $\mathbf{F}_i^{\mathrm{ex}} = \mathbf{f}_i^{\mathrm{ex}} - \nabla_i U^{\mathrm{ex}}$ is an arbitrary externally applied one-body force that can contain conservative ($-\nabla_i U^{\mathrm{ex}}$) and nonconservative contributions ($\mathbf{f}_i^{\mathrm{ex}}$). A possible dependence on particle positions is implied by the index. The second process governs particle orientations undergoing free rotational diffusion, whereby the inverse timescale for particle reorientation is given by the rotational diffusion coefficient D_{r}. The associated dynamics is governed by $\Delta_{\mathbf{e}_i}$, which denotes the spherical Laplace operator in d dimensions that acts on the orientation of the ith particle. Finally, the third process involves the effective chemical events due to which particles are displaced by the distance λ along their orientation for each successful reaction (Fig. 3). These active translations are captured by the discrete difference operator

$$\widehat{\nabla}_i j_i^{\mathrm{c}} \equiv j_i^{\mathrm{c}}(\mathbf{r}_i, n_i) - j_i^{\mathrm{c}}(\mathbf{r}_i - \lambda \mathbf{e}_i, n_i - 1), \tag{14}$$

where we define the particle-resolved chemical currents

$$j_i^{\mathrm{c}} \equiv \Psi(\mathbf{r}_i, n_i) k_i^+(\mathbf{r}_i) - \Psi(\mathbf{r}_i + \lambda \mathbf{e}_i, n_i + 1) k_i^-(\mathbf{r}_i + \lambda \mathbf{e}_i). \tag{15}$$

To improve readability, only the arguments that change in transitions are indicated. It is important to note that these chemical currents simultaneously convey changes in particle positions (along their orientations) and the net number of chemical events $\{n_i\}$. As seen later, they give rise to the chemical flux $\mathcal{J}$ between substrate and product reservoirs, which constitutes the work input.

Collecting all terms, the N-body joint distribution $\Psi(\mathbf{r}^N, \mathbf{e}^N, n^N; t)$ then obeys the exact evolution equation

$$\frac{\partial \Psi}{\partial t} = -\sum_{i=1}^{N} \{\nabla_i \cdot \mathbf{j}_i^{\mathrm{p}} - D_{\mathrm{r}} \Delta_{\mathbf{e}_i} \Psi + \widehat{\nabla}_i j_i^{\mathrm{c}}\}. \tag{16}$$

Hence, the dynamics follows an augmented Smoluchowski, or, equivalently, Fokker-Planck, equation of interacting Brownian particles that undergo discrete stochastic jumps by locally catalyzing chemical events.

2. Dissipated heat

We can now apply the standard framework of stochastic thermodynamics to identify the dissipation. To this end, it is instructive to consider infinitesimal increments for a single active particle. The first law of thermodynamics reads $đq = đw - \mathrm{d}U$, where throughout we adopt the convention that work applied to the system and heat dissipated into the surrounding medium take positive values. We split the stochastic first law for each particle into (i) displacements caused by the total force $\mathbf{F}_i^{\mathrm{ex}} - \nabla_i U$ and (ii) chemically induced displacements along its orientation. For (i), work $đw_i^{\mathrm{p}} = \mathbf{F}_i^{\mathrm{ex}} \circ \mathrm{d}\mathbf{r}_i^{\mathrm{p}}$ is performed by the external force with infinitesimal displacement $\mathrm{d}\mathbf{r}_i^{\mathrm{p}}$. Throughout, we work in the Stratonovich convention [157] and denote corresponding (inner) products by "$\circ$". The associated change in internal energy U is captured by the shift in potential energy $\mathrm{d}U_i^{\mathrm{p}} = \nabla_i U \circ \mathrm{d}\mathbf{r}_i^{\mathrm{p}}$, from which follows the dissipated heat

$$đq_i^{\mathrm{p}} = đw_i^{\mathrm{p}} - \mathrm{d}U_i^{\mathrm{p}} = (\mathbf{F}_i^{\mathrm{ex}} - \nabla_i U) \circ \mathrm{d}\mathbf{r}_i^{\mathrm{p}}. \tag{17}$$

The extension to N particles is straightforward and, following the standard procedure of stochastic thermodynamics [66], allows us to express the average dissipated heat per unit of time:

$$\dot{Q}^{\mathrm{p}} \equiv \sum_{i=1}^{N} \int \mathrm{d}\mathbf{r}^N \mathrm{d}\mathbf{e}^N \mathrm{d}n^N \mathbf{j}_i^{\mathrm{p}} \cdot (\mathbf{F}_i^{\mathrm{ex}} - \nabla_i U), \tag{18}$$

stemming from particle displacements due to the forces exerted onto them. To prevent notational clutter, $\int \mathrm{d}\mathbf{r}^N \mathrm{d}\mathbf{e}^N \mathrm{d}n^N$ denotes integration over positions, orientations, and summation over the number of chemical events across all N particles.

For the chemical events, the work increment splits into two contributions:

$$đw_i^{\mathrm{c}} = \Delta\mu + \int_0^{\lambda} \mathrm{d}\ell\, \mathbf{e}_i \cdot \mathbf{F}_i^{\mathrm{ex}}(\mathbf{r}_i + \ell \mathbf{e}_i). \tag{19}$$

The first contribution describes the work injected in the form of chemically liberated free energy, whereas the second captures the mechanical work to displace the particle by a distance λ along its orientation. The corresponding change in internal energy reads $\mathrm{d}U_i^{\mathrm{c}} = U(\mathbf{r}_i + \lambda \mathbf{e}_i) - U(\mathbf{r}_i)$, which results in the dissipated heat associated with a single chemical event $đq_i^{\mathrm{c}} = đw_i^{\mathrm{c}} - \mathrm{d}U_i^{\mathrm{c}}$. This dissipation constrains the forward and backward rates through the local detailed balance condition [cf. Eq. (8)]

$$\frac{k_i^+(\mathbf{r}_i)}{k_i^-(\mathbf{r}_i + \lambda \mathbf{e}_i)} = e^{\beta đq_i^{\mathrm{c}}}, \tag{20}$$

one of the cornerstones of stochastic thermodynamics. In essence, it intertwines the systems dynamics and energetics by reducing (enhancing) the probability to observe state changes associated with an increase (decrease) in potential energy. In analogy with Eq. (18), we thus identify

$$\dot{Q}^{\mathrm{c}} \equiv \sum_{i=1}^{N} \int \mathrm{d}\mathbf{r}^N \mathrm{d}\mathbf{e}^N \mathrm{d}n^N j_i^{\mathrm{c}} k_{\mathrm{B}} T \ln \frac{k_i^+}{k_i^-} \tag{21}$$

as the average heat rate caused by (local) dissipation of chemically liberated free energy and the associated particle translations along their respective orientations. The total dissipation rate of the system is given by the superposition $\dot{Q} = \dot{Q}^{\mathrm{p}} + \dot{Q}^{\mathrm{c}}$. Our result holds for idealized chemostats, i.e., constant $\Delta\mu$. In case of nonconstant affinity, chemical reservoirs undergo a change in entropy yielding an additional contribution to the dissipation (for a comprehensive discussion, see Ref. [68]). Notably, rotational diffusion does not contribute to the dissipation due to its time-reversal symmetry.

3. Coarse-graining chemical events

Inspecting the results of the previous section (Sec. III B 1) closer, we see that the net number of chemical events n_i are needed for bookkeeping but can be eliminated due to the tight coupling between such events and active displacements. To this end, we expand

$$\Psi(\mathbf{r}_i \pm \lambda \mathbf{e}_i, n_i \pm 1) \approx \Psi(\mathbf{r}_i \pm \lambda \mathbf{e}_i, n_i) \pm \partial_{n_i} \Psi(\mathbf{r}_i \pm \lambda \mathbf{e}_i, n_i), \tag{22}$$

assuming real valued n_i for simplicity. Note that, in doing so, we implicitly invoke two assumptions: (i) The time increment of consecutive observations $\mathrm{d}t$ is required to be sufficiently small, such that reaction coordinates $\{n^N\}$ are essentially statistically independent Poisson random variables. (ii) Simultaneously, $\mathrm{d}t$ has to be long enough to assure the occurrence of a large number of reactions within $[t, t + \mathrm{d}t]$. Upon satisfying the latter condition, integer Poisson variables are well approximated by real-valued Gaussian random variables, by virtue of the central limit theorem [158]. Upon integrating

$$\psi(\mathbf{r}^N, \mathbf{e}^N; t) = \int \mathrm{d}n^N \Psi(\mathbf{r}^N, \mathbf{e}^N, n^N; t), \tag{23}$$

the state of the system is described by the collection $\{\mathbf{r}^N, \mathbf{e}^N\}$ of particle positions and orientations with joint probability $\psi(\mathbf{r}^N, \mathbf{e}^N; t)$.

To proceed, we exploit the fact that λ is a microscopic length scale which is much smaller than the size of colloidal particles (cf. Sec. II). We assume explicit expressions for the transition rates, for which we again choose a symmetric form

$$k_i^{\pm} \equiv \kappa^{\pm} e^{(\beta/2)[-U(\mathbf{r}_i \pm \lambda \mathbf{e}_i) + U(\mathbf{r}_i) \pm \lambda \mathbf{e}_i \cdot \mathbf{F}_i^{\mathrm{ex}}]}, \tag{24}$$

with rates $\kappa^{\pm}$ for a free particle [Eq. (11)] so that local detailed balance [Eq. (20)] is satisfied. We note that an alternative choice of rates, similar to the one in Eq. (7), leaves the results of the following calculation unchanged (for details, see Appendix B).

We expand the joint distribution [Eq. (23)] and transition rates [Eq. (24)] at leading order in λ, the details of which can be found in Appendix C 1. In doing so, the discrete difference operator [Eq. (14)] becomes

$$\widehat{\nabla}_i j_i^{\mathrm{c}} = \lambda \mathbf{e}_i \cdot \nabla_i j_i^{\mathrm{c}}, \tag{25}$$

where we identify the continuous chemical current

$$j_i^{\mathrm{c}} \equiv \frac{v_i}{\lambda} \psi - \frac{D^{\mathrm{c}}}{\lambda} \mathbf{e}_i \cdot \nabla_i \psi + \mathcal{O}(\lambda^2). \tag{26}$$

Note that the speed $v_i \equiv v_0 + \mu^{\mathrm{c}} \mathbf{e}_i \cdot (\mathbf{F}_i^{\mathrm{ex}} - \nabla_i U)$ acquires a nonconstant, position-dependent contribution, with v_0 given in Eq. (10) and chemical mobility $\mu^{\mathrm{c}} \equiv \beta D^{\mathrm{c}} \propto \lambda^2$ [Eq. (12)].

By plugging Eq. (26) into Eq. (16) and truncating the small-λ expansion at first order, the N-body Smoluchowski equation reduces to

$$\frac{\partial \psi}{\partial t} = -\sum_{i=1}^{N} \{\nabla_i \cdot \mathbf{j}_i - D_{\mathrm{r}} \Delta_{\mathbf{e}_i} \psi\} \tag{27}$$

with the current

$$\mathbf{j}_i \equiv [v_0 \mathbf{e}_i + \mu_0 (\mathbf{F}_i^{\mathrm{ex}} - \nabla_i U) - D_0 \nabla_i] \psi \tag{28}$$

associated with the ith particle. Equation (27) is the evolution equation of active particles that are propelled with constant speed v_0. In the literature, this model is commonly referred to as *active Brownian particles* (ABPs), a well-studied paradigm in active matter research [17,18,20,22,42,46,159–161]. The novelty of our approach is that information about the underlying self-propulsion mechanism directly enters through the self-propulsion speed v_0 in the form of the effective attempt rate k_{eff}, the chemical potential difference $\Delta\mu$, and the displacement length λ. Moreover, necessary thermodynamic details are directly encoded in the chemical currents [Eq. (26)], which we exploit in the following section to extract the exact dissipation rate.

Before moving on, we emphasize that, when studying the *dynamical* collective behavior of ABPs, it is sufficient to model individual particles to exhibit a constant self-propulsion speed (sometimes also interpreted as an active force [43,108,162,163]) without specifying its underlying origin. It is important to realize, however, that this approach is not suited to study thermodynamic properties. Some

previous studies have identified this problem and proposed more detailed models for the directed motion of catalytic particles. Approaches include modeling self-diffusiophoretic forces [137,140,141], introducing effective chemical events that, similar to the discrete motion of molecular motors [63,164,165], displace particles between adjacent lattice sites [138]—the same idea was developed for the off-lattice description introduced in Sec. III B 1 [139]—and, more recently, the embedding of active particle models into two temperature processes [166].

4. Mesoscopic dissipation rate

We now consider steady states defined by a time-independent joint probability $\psi(\mathbf{r}^N, \mathbf{e}^N)$. To calculate the dissipation rate, we insert the particle current [Eq. (13)] and the chemical current [Eq. (26)] into the respective contribution to the total dissipation [Eqs. (18) and (21)]. The first takes the form

$$\dot{Q}^{\mathrm{p}} = \sum_{i=1}^{N} \int \mathrm{d}\mathbf{r}^N \mathrm{d}\mathbf{e}^N [\mu_0 (\mathbf{F}_i^{\mathrm{ex}} - \nabla_i U)^2 \psi - D_0 (\mathbf{F}_i^{\mathrm{ex}} - \nabla_i U) \cdot \nabla_i \psi], \tag{29}$$

which is generally nonzero except in thermal equilibrium when ψ is Boltzmann distributed. The associated rate of dissipation due to effective chemical events

$$\dot{Q}^{\mathrm{c}} = \sum_{i=1}^{N} \int \mathrm{d}\mathbf{r}^N \mathrm{d}\mathbf{e}^N \left[\frac{v_0}{\lambda} \Delta\mu\psi + v_0 \mathbf{e}_i \cdot (\mathbf{F}_i^{\mathrm{ex}} - \nabla_i U)\psi + \frac{\mu^{\mathrm{c}}}{\lambda} \Delta\mu \mathbf{e}_i \cdot (\mathbf{F}_i^{\mathrm{ex}} - \nabla_i U)\psi - \Delta\mu \frac{D^{\mathrm{c}}}{\lambda} \mathbf{e}_i \cdot \nabla_i \psi \right] \tag{30}$$

follows by additionally plugging the local detailed balance condition [Eq. (20)] into Eq. (21) and discarding terms beyond linear order in λ to be consistent with the limit in which ABPs emerge.

By rewriting Eqs. (29) and (30), we show in Appendix C 2 that all terms involving a conservative force as affinity become boundary terms and, thus, do not contribute to the average global dissipation rate

$$\dot{Q} = \sum_{i=1}^{N} \int \mathrm{d}\mathbf{r}^N \mathrm{d}\mathbf{e}^N (j_i^{\mathrm{c}} \Delta\mu + \mathbf{j}_i \cdot \mathbf{f}_i^{\mathrm{ex}}). \tag{31}$$

From the first term, we identify the solute flux due to the ith particle as $\mathcal{J}_i \equiv \int \mathrm{d}\mathbf{r}^N \mathrm{d}\mathbf{e}^N (v_i/\lambda)\psi$. Importantly, we thus find that the dissipated heat is given by the net number of chemical conversions $\mathcal{J} = \sum_i \mathcal{J}_i$ times the liberated free energy $\Delta\mu$ per event, plus the mechanical work that is performed by nonconservative external forces. While this result should have been anticipated (cf. Ref. [135] for a single chemically driven particle), we have shown it explicitly from the definition of the dissipated heat [Eqs. (18) and (21)] and the evolution of the joint probability [Eq. (16)]. We emphasize that both flux and speed are related by $\langle v_i \rangle = \lambda \mathcal{J}_i$.

Before turning toward a macroscopic description in the next section, let us briefly comment on how the underlying solute degrees of freedom influence the dissipation rate. To this end, consider the case of a fixed chemical potential difference $\Delta\mu$ and speed v_0, which imposes $\lambda k_{\mathrm{eff}} = \mathrm{const}$ [cf. Eq. (10)]. Since properties of the molecular solutes enter the mesoscopic dynamics [Eq. (27)] only through v_0, they remain unaltered. In contrast, the dissipation rate [Eq. (31)] is sensitive to changes of λ and k_{eff}, since maintaining a constant speed for, e.g., smaller λ has to be compensated by an increased attempt frequency and, thus, solute flux. This, in turn, implies a larger thermodynamic cost to maintain the directed motion [see Eq. (31)]. A previous study had considered active particles moving on a lattice [138], where diffusive particle displacement and chemical steps are coupled through the same lattice constant, leading to closed expressions in the continuum limit. This is not the case when explicit chemical events are considered off lattice, leading to a small jump length λ defined through microscopic interactions [cf. Eq. (5)]. We discuss implications that would follow an *a priori* truncation of the chemical current in Appendix C 1 b.

C. The hydrodynamic scale: Dissipation from fields

1. Coarse-graining

Thus far, we restricted ourselves to the discussion of particle-resolved models. Now, we want to go one step further by turning toward a field-theoretic description of both the dynamics and thermodynamics of the system at hand by deriving effective hydrodynamic equations while simultaneously extracting the corresponding thermodynamically consistent dissipation rate. To this end, we employ the explicit coarse-graining scheme introduced by Bialké, Löwen, and Speck [53].

Starting with the evolution equation of the joint distribution in Eq. (27), we adopt an effective one-particle picture by integrating over positions and orientations of all but one (tagged) particle. Since all particles are assumed to be identical, we designate $i = 1$ as the tagged particle and drop subscripts from here on out. Subsequently, the equation of motion of the marginal one-point particle density $\psi_1(\mathbf{r}, \mathbf{e}; t)$ takes the form

$$\frac{\partial \psi_1}{\partial t} = N \int \mathrm{d}\mathbf{r}^{N-1} \mathrm{d}\mathbf{e}^{N-1} \frac{\partial \psi}{\partial t} = -\nabla \cdot [v_0 \mathbf{e} + \mu_0 (\mathbf{F}^{\mathrm{ex}} + \mathbf{F}) - D_0 \nabla] \psi_1 + D_{\mathrm{r}} \Delta_{\mathbf{e}} \psi_1. \tag{32}$$

Here, $\mathbf{F}$ describes the forces exerted on the tagged particle due to particle interactions. In the case of pairwise

interactions, these couple to $\psi_2(\mathbf{r}'|\mathbf{r},\mathbf{e};t)$, the density to find a second particle at position $\mathbf{r}'$ conditioned on the tagged particle being at $\mathbf{r}$ with orientation $\mathbf{e}$ at time t. Thus, the (conditional) interaction forces are given by

$$\mathbf{F} = \int \mathrm{d}\mathbf{r}'\, \mathbf{f}(\mathbf{r}-\mathbf{r}')\psi_2(\mathbf{r}'|\mathbf{r},\mathbf{e};t) \tag{33}$$

with two-body force $\mathbf{f} = -\nabla u$ for the pair potential $u(r)$ between the active colloidal particles. To complete the coarse-graining, we introduce order parameter fields as moments of the particle orientation—namely, the local density $\rho(\mathbf{r},t) \equiv \int \mathrm{d}\mathbf{e}\,\psi_1$ and the polarization density $\mathbf{p}(\mathbf{r},t) \equiv \int \mathrm{d}\mathbf{e}\,\mathbf{e}\psi_1$, alongside higher moments—and calculate their evolution equations by plugging Eq. (32) into the time derivatives of their respective definition. In doing so, we obtain an infinite hierarchy of coupled equations [167], reminiscent of the Bogoliubov-Born-Green-Kirkwood-Yvon hierarchy in kinetic theory [168]. The density obeys the continuity equation

$$\frac{\partial\rho}{\partial t} = -\nabla\cdot\mathbf{j} \tag{34}$$

with one-body particle current

$$\mathbf{j}(\mathbf{r},t) = v_0\mathbf{p} + \mu_0(\rho\mathbf{F}^{\mathrm{ex}} + \nabla\cdot\boldsymbol{\sigma}). \tag{35}$$

Here, we identify the symmetric stress tensor $\boldsymbol{\sigma} = -k_{\mathrm{B}}T\rho\mathbf{1} + \boldsymbol{\sigma}_{\mathrm{IK}}$ by defining the Irving-Kirkwood tensor $\boldsymbol{\sigma}_{\mathrm{IK}}$ through $\nabla\cdot\boldsymbol{\sigma}_{\mathrm{IK}} = \langle\mathbf{F}\rangle_{\mathbf{r}}$ [169] (where $\langle\cdot\rangle_{\mathbf{r}}$ denotes averages over the tagged particle orientation). Equation (35) describes the generalized hydrostatic force balance of a nonequilibrium steady state and reduces to the mechanical equilibrium condition $\nabla\cdot\boldsymbol{\sigma} = 0$ for the nondriven case [54]. In contrast, higher-order fields, like the local polarization density following the evolution equation:

$$\frac{\partial\mathbf{p}}{\partial t} = -\nabla\cdot\left[\frac{v_0}{d}\rho\mathbf{1} + v_0\mathbf{Q} + \mu_0(\mathbf{p}\mathbf{F}^{\mathrm{ex}} + \langle\mathbf{e}\mathbf{F}\rangle_{\mathbf{r}}) - D_0\nabla\mathbf{p}\right] - D_{\mathrm{r}}\mathbf{p}, \tag{36}$$

are generally nonconserved and decay increasingly fast with characteristic decay rates $\propto D_{\mathrm{r}}$ [70]. Here, $\mathbf{Q} = \int \mathrm{d}\mathbf{e}(\mathbf{e}\mathbf{e} - \mathbf{1}/d)\psi_1$ is the nematic tensor, and we denote direct products as $(\mathbf{a}\mathbf{b})_{ij} = a_i b_j$. Since each evolution equation couples to the next higher-order moment, an approximate closure is needed to truncate the hierarchy of equations. For the dissipation, however, general results are attainable at the level of density and polarization without introducing further assumptions.

2. Macroscopic dissipation rate

To arrive at an expression for the steady state dissipation rate of such macroscopic fields, we repeat the exact same coarse-graining procedure for the global dissipation rate of ABPs given by Eq. (31). In contrast to the previously discussed particle-resolved dynamics, where extending the domain over the full system implied vanishing boundary terms (cf. Appendix C 2), treatment on the level of hydrodynamic equations enables the study of subsystems without contradicting mass conservation.

The macroscopic dissipation rate associated with a (sub)region Ω [cf. Fig. 4(a)] takes the form

$$\dot{Q}_\Omega = \int_\Omega \mathrm{d}\mathbf{r}(j^{\mathrm{c}}\Delta\mu + \mathbf{j}\cdot\mathbf{f}^{\mathrm{ex}}) + \oint_{\partial\Omega}\mathrm{d}A\,\mathbf{n}\cdot\mathbf{J} \tag{37}$$

with macroscopic local chemical current

$$j^{\mathrm{c}}(\mathbf{r}) = \frac{v_0}{\lambda}\rho + \frac{\mu^{\mathrm{c}}}{\lambda}(\mathbf{p}\cdot\mathbf{F}^{\mathrm{ex}} + \langle\mathbf{e}\cdot\mathbf{F}\rangle_{\mathbf{r}}) - \frac{D^{\mathrm{c}}}{\lambda}\nabla\cdot\mathbf{p} \tag{38}$$

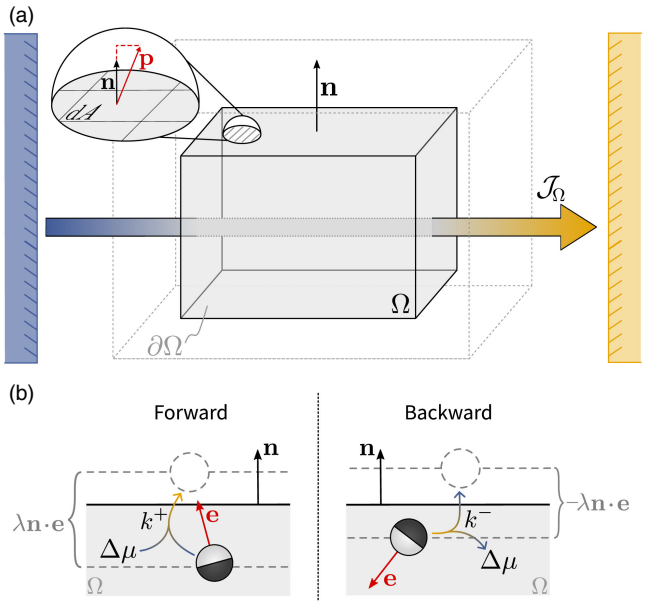

FIG. 4. Subsystems and boundary fluxes. (a) Sketch of a subsystem Ω bounded by the surface $\partial\Omega$. The shaded arrow indicates the average chemical flux $\mathcal{J}_\Omega$ from the substrate reservoir (blue, left) to the product reservoir (yellow, right). The red arrow indicates the polarization $\mathbf{p}$ on the boundary. Projecting $\mathbf{p}$ onto the outward-facing normal vector $\mathbf{n}$ and integrating over the infinitesimal surface element $\mathrm{d}A$ gives the boundary contribution $\dot{\Gamma}_\Omega$ for the dissipation rate. (b) Caricature illustrating the effect of a boundary on the dissipation rate. Every forward reaction (left) that pushes the particle out of Ω transfers $\Delta\mu$ to the surrounding medium. Backward reactions (right) replenish a $\Delta\mu$ to the chemostat, and associated boundary crossings are not accompanied by heat transport. The difference of both processes (and the analog for particles entering the subdomain) leads to the average boundary flux Eq. (40).

obtained from Eq. (26). The spatial integral of this chemical current produces two terms, the chemical flux

$$\mathcal{J}_\Omega = \int_\Omega \mathrm{d}\mathbf{r}\left[\frac{v_0}{\lambda}\rho + \frac{\mu^c}{\lambda}(\mathbf{p}\cdot\mathbf{F}^{\mathrm{ex}} + \langle \mathbf{e}\cdot\mathbf{F}\rangle_{\mathbf{r}})\right] \tag{39}$$

and a boundary term

$$\dot{\Gamma}_\Omega = \frac{\lambda}{2}(\kappa^+ + \kappa^-)\oint_{\partial\Omega} \mathrm{d}A\, \mathbf{n}\cdot\mathbf{p} \tag{40}$$

that captures the mismatch between the work extracted from the chemostat and dissipation due to directed particle motion. In order to recover the global dissipation rate Eq. (31) when extending Ω to the full system, any further contribution can enter only as a boundary term, i.e., as a dissipation flux $\mathbf{J}(\mathbf{r})$. Such a redistribution of dissipation apparently arises through conservative forces (cf. Appendix C 2), for which explicit expressions are challenging to obtain through systematic coarse-graining. However, we posit that dissipation from conservative forces is strictly local and, thus, $\mathbf{J} = 0$ in this system. To corroborate this argument, let us assume that there is a nonvanishing one-body potential U^{ex}, for which $\mathbf{J} = -\mathbf{j}U^{\mathrm{ex}}$ (Appendix C 2). Adding a constant to this potential does not change forces but would imply a change in dissipation within Ω. As this term simply transfers energy elsewhere in the system rather than dumping it into the heat reservoir, we conclude $\mathbf{J} = 0$.

On the other hand, the emergence of a boundary term in the form of Eq. (40) can be rationalized as follows [cf. Fig. 4(b)]: Assume that particles located at the boundary $\partial\Omega$ are aligned with the normal vector $\mathbf{n}$, i.e., $\dot{\Gamma}_\Omega > 0$. In order to perform a reactive step, particles extract work from the chemostat while still inside Ω. However, by performing the step, they exit the subsystem, thereby transferring this energy into the surroundings as heat. As a result, the amount of heat dissipated by Ω decreases by the exact rate of effectively transferred heat $\dot{Q}^{\mathrm{tr}}_\Omega = \dot{\Gamma}_\Omega\Delta\mu$, maintaining energy conservation of the composite system. Analogously, for $\dot{\Gamma}_\Omega < 0$ the dissipation rate of Ω increases. Note that we recover the first law of thermodynamics on the level of active fields, since Eq. (37) equates the rate of heat dissipation in any subsystem $\dot{Q}_\Omega$ with the difference between the rate of work $\dot{\mathcal{W}}^{\mathrm{in}}_\Omega = \mathcal{J}_\Omega\Delta\mu + \int_\Omega \mathrm{d}\mathbf{r}\,\mathbf{j}\cdot\mathbf{f}^{\mathrm{ex}}$ injected into the region Ω and the rate $\dot{Q}^{\mathrm{tr}}_\Omega = \dot{\Gamma}_\Omega\Delta\mu$ with which heat is transferred between Ω and its surrounding. Since the last contribution is solely determined by local polar order at the subsystem boundary [see Eq. (40)], its presence (or absence) generally relies on the system geometry and the specific choice of subsystem Ω (see Sec. IV A).

Putting everything together, we conclude that the local dissipation rate is unambiguous and reads

$$\dot{q}(\mathbf{r}) = j^c(\mathbf{r})\Delta\mu + \mathbf{j}\cdot\mathbf{f}^{\mathrm{ex}} \tag{41}$$

with $j^c(\mathbf{r})$ as given in Eq. (38) and the particle current of Eq. (35). While mathematically there is an apparent gauge freedom $\dot{q} \to \dot{q} + \nabla\cdot\mathbf{J}$ under which $\dot{Q}$ remains invariant, physical arguments assert $\mathbf{J} = 0$. As we illustrate in Sec. IV, Eq. (41) allows one to unveil inhomogeneities in the dissipation rate due to local features, such as, e.g., confinements or interfaces between coexisting phases.

IV. ILLUSTRATIONS

A. Flat wall

To get a better understanding of Eq. (37) and its components [Eqs. (39) and (40)], it is instructive to consider a simple, analytically solvable example and explicitly calculate its dissipation rate. To this end, we consider a two-dimensional system in the presence of a flat wall positioned at $x = 0$ [see Fig. 5(a)]. For simplicity, we assume noninteracting particles and close the hierarchy of hydrodynamic equations at the nematic order by setting

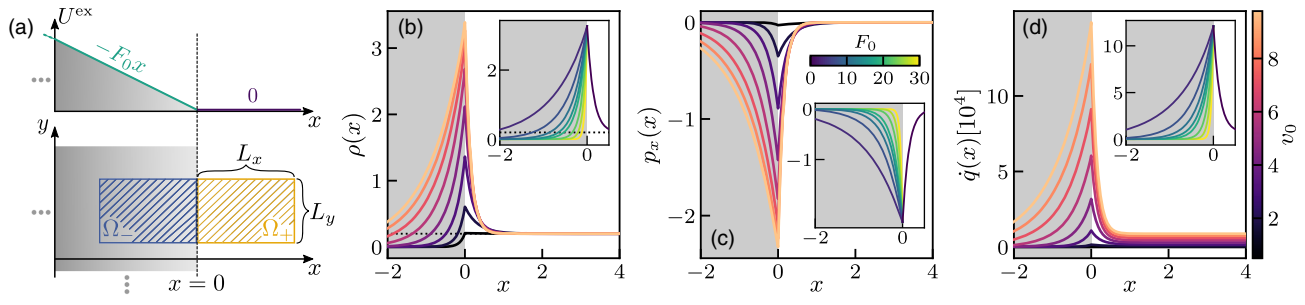

FIG. 5. Catalytic particles in the presence of a straight potential wall. (a) Sketch of the considered system, where for $x < 0$ (shaded gray regions) particles experience a constant force due to the wall potential $U^{\mathrm{ex}} = -F_0x$ and are freely moving for $x > 0$. The bottom axis shows subsystems $\Omega_\pm$ of same size $L_x \times L_y$, sharing a boundary at $x = 0$. (b) Density profiles $\rho(x)$, (c) polarization profiles $p_x(x)$, and (d) the local dissipation rate $\dot{q}(x)$ for $F_0 = 8$. Colors correspond to different self-propulsion speeds v_0 obtained by varying $\Delta\mu$ (and setting $\lambda = 10^{-3}$ with $k_{\mathrm{eff}}\lambda = 5$). Insets depict the respective profiles for a fixed value of $v_0 \approx 9.6$ with varying F_0, as indicated by the colors. The dotted black line in (b) shows the bulk density $\rho_b = 0.2$.

$\mathbf{Q} \approx 0$. Throughout we report values of quantities as dimensionless by measuring lengths in units of particle diameters σ, energies in units of $k_B T$, and times in units of σ^2/D_0. Moreover, we set the rotational diffusion coefficient to $D_r = 3D_0/\sigma^2$, as is customary for hard disks due to the no-slip boundary of colloidal particles [20,170]. For equations, we retain proper dimensions.

In the $x > 0$ region, particles are freely self-propelling and experience no forces. For $x < 0$, particles experience a constant force of strength F_0 directed along x due to the linear potential $U^{\mathrm{ex}} = -F_0 x$. Hence, the limit $F_0 \to \infty$ results in a hard wall. Note that by construction the system is symmetric along y, allowing us to write density $\rho(x)$ and nonzero polarization component $p_x(x)$ as functions of x only. Additionally, $\mathbf{j} = 0$ in steady state. The solutions are derived in Appendix D and given by Eqs. (D8) and (D9), with coefficients in Eq. (D10). A visual representation is provided by Figs. 5(b) and 5(c) for different self-propulsion speeds and force strengths (see insets). The results agree with the known trend that motile particles have the tendency to aggregate at walls with polar alignment perpendicular to the boundary [171–173]. Upon increasing the force strength, exploration of the negative half-space is suppressed, leading to steeper exponential decays in both density and associated polarization.

Using Eq. (41), we calculate the local dissipation rate [see Fig. 5(d)], which upon comparison with Fig. 5(b) clearly shares the characteristics of the density profile as expected. We emphasize that the exact values displayed in Fig. 5(d) are highly sensitive to the choice of k_{eff} and λ. Since the self-propulsion speed v_0 [Eq. (10)] is restricted to values in the interval $v_0 \in [-2k_{\mathrm{eff}}\lambda, 2k_{\mathrm{eff}}\lambda]$, due to the bounded hyperbolic tangent, the range of attainable speeds is determined by the product $k_{\mathrm{eff}}\lambda$. For instance, by fixing $k_{\mathrm{eff}}\lambda = 5$ as is done for Fig. 5, speeds saturate at a value of $v_0 = 10$. Moreover, by fixing $k_{\mathrm{eff}}\lambda$ the magnitude of the density-dependent term scales inversely with λ; i.e., if chemically induced displacements are short, maintaining a speed v_0 requires additional reactions which further promotes the dominance of the density-dependent source term in Eq. (38). Nonetheless, the discussed trend is representative for physically sensible parameter choices.

Near the wall, locally induced polar order contributes to the dissipation rate in two ways. First, for $x > 0$ ($x < 0$), the positive (negative) divergence of polarization $\mathbf{p}$ [see the last term in Eq. (38)] reduces (enhances) dissipation. Second, the strong antialignment between forces acting in the negative half-space and the polarization field lead to an additional negative contribution for $x < 0$. This demonstrates that boundaries and obstacles play highly nontrivial roles in shaping the system's dissipation. Regardless, the dominant source term overshadows these intricacies due to the greatly increased local density by particles aggregating at the wall.

Note that the dissipation rate is well defined anywhere but $x = 0$ due to the cusp in the polarization field. Both limits $\dot{q}(x \to \pm 0)$, however, exist. For $x \to -\infty$, dissipation vanishes due to the absence of particles, and for $x \to \infty$ it converges to the constant bulk value $\dot{q}(x \to \infty) = v_0 \rho_b \Delta\mu/\lambda$.

We now shift our attention to the finite subsystems $\Omega_\pm$ of area $L_x \times L_y$ that share a boundary at $x = 0$, as depicted in Fig. 5(a), and calculate the respective average total dissipation rates $\dot{Q}_\pm = (\mathcal{J}_\pm - \dot{\Gamma}_\pm)\Delta\mu$. Assuming sufficiently large L_x, such that $\rho(L_x) \approx \rho_b$ and $\rho(-L_x) \approx 0$, the only contribution to the contour integral in Eq. (40) stems from the shared boundary at $x = 0$, since polar order vanishes in the bulk and $p_y = 0$. Consequently, for $x > 0$, one obtains Eq. (D11) for the average solute flux and

$$\dot{\Gamma}_+ = -\frac{D^c}{\lambda}\int_0^{L_y} \mathrm{d}y\, p_x(0) = \frac{D^c}{\lambda}\frac{D_0 C_+}{v_0 \xi} L_y \tag{42}$$

for the boundary term with decay length $\xi \equiv \sqrt{D_0/D_r}/\sqrt{1 + v_0^2/(2D_r D_0)}$ and coefficient $C_+ = \rho_b v_0^2/(2D_r D_0)$. Similarly, for $x < 0$, we find the solute flux [Eq. (D12)] and the boundary contribution

$$\dot{\Gamma}_- = -\frac{D^c}{\lambda}\frac{D_0 C_+}{v_0 \xi} L_y = -\dot{\Gamma}_+. \tag{43}$$

Notably, all contributions individually vanish in equilibrium ($\Delta\mu = 0$). Moreover, $\dot{\Gamma}_-$ is given by its positive half-space counterpart $\dot{\Gamma}_+$ under change of sign, indicating the exchange of heat between the two subsystems. More precisely, in this example, Ω_+ transfers heat with rate $\dot{Q}_+^{\mathrm{tr}} = \dot{\Gamma}_+ \Delta\mu$—that was originally extracted in the form of chemical work from the chemostat—to the neighboring subsystem Ω_-, mediated by the nonzero polarization at the shared boundary along $x = 0$. Consequently, obstacles or confinements that induce local polar order can, depending on the specific choice of subsystem, take the role of either a dissipation sink (Ω_+) or source (Ω_-). Crucially, the energy of the composite system is still conserved, as these effects vanish for bulk averages. This can be seen by, e.g., considering the combined system $\Omega = \Omega_+ + \Omega_-$. For the combined energy balance, boundary contributions cancel each other, resulting in the first law $\dot{Q}_\Omega = (\mathcal{J}_+ + \mathcal{J}_-)\Delta\mu = \mathcal{W}_\Omega^{\mathrm{in}}$, which assures the conservation of energy by equating the rates of heat dissipation and work injection.

B. Motility-induced phase separation—MIPS

As a second example, we consider a suspension of interacting motile particles that exhibits MIPS [20,22,46] and compute its spatially resolved dissipation rate. This allows us to uncover the mechanisms contributing

to heat dissipation and characterize the role of local energy consumption to maintaining the nonequilibrium phase coexistence.

We analyze simulation data of $N = 4000$ active colloids in a periodic $L \times L$ square box, with $L \approx 102.3$ and a packing fraction of $\phi = 0.3$. Particles interact via a repulsive Weeks-Chandler-Anderson potential, and we apply no external force: $\mathbf{F}^{\mathrm{ex}} = 0$ (for details, see Appendix F 2). Measuring quantities in the same units as in the proceeding section (Sec. IV A), particles are self-propelled with speed $v_0 = 80$ and, consequently, undergo MIPS as predicted from the well-explored phase diagram of ABPs [160,170,174]. A simulation snapshot of the phase coexistence is shown in Fig. 6(a). By averaging binned data over several time steps, we obtain the coarse-grained hydrodynamic fields depicted in Fig. 6(b), where colors indicate the density and arrows the polarization field. Arrows are scaled proportional to the polarization magnitude and indicate polar ordering at the liquid-gas interface.

Using Eq. (41), the local dissipation rate amounts to the values displayed in Figs. 6(c) and 6(e). Here, we use $\lambda = 10^{-3}$, set $k_{\mathrm{eff}}\lambda = 50$, and emphasize that the following discussion is representative for physically sensible parameter choices, namely, $\lambda \ll \sigma$. In analogy with the results obtained in Sec. IV A, heat dissipation is largely determined by the density-dependent housekeeping contribution, i.e., the first term of Eq. (38) that enters Eq. (41). We emphasize that this term is not conditioned on particle displacements *per se*, which means that, although active translations are inhibited, colloids arrested in the dense cluster maintain persistent fuel consumption. Consequently, the local dissipation is maximal within the dense domain.

In close vicinity of the interface, the strong anticorrelation between particle orientations (pointing toward the cluster center) and repulsive interaction forces (pointing outward), i.e., $\langle \mathbf{e} \cdot \mathbf{F} \rangle_{\mathbf{r}} < 0$, decreases the chemical current. If one corrects for the housekeeping term, the residual heat rate $\dot{q}^{\mathbf{p}} \equiv \dot{q} - v_0 \Delta\mu\rho/\lambda$ forms a ring along the cluster boundary,

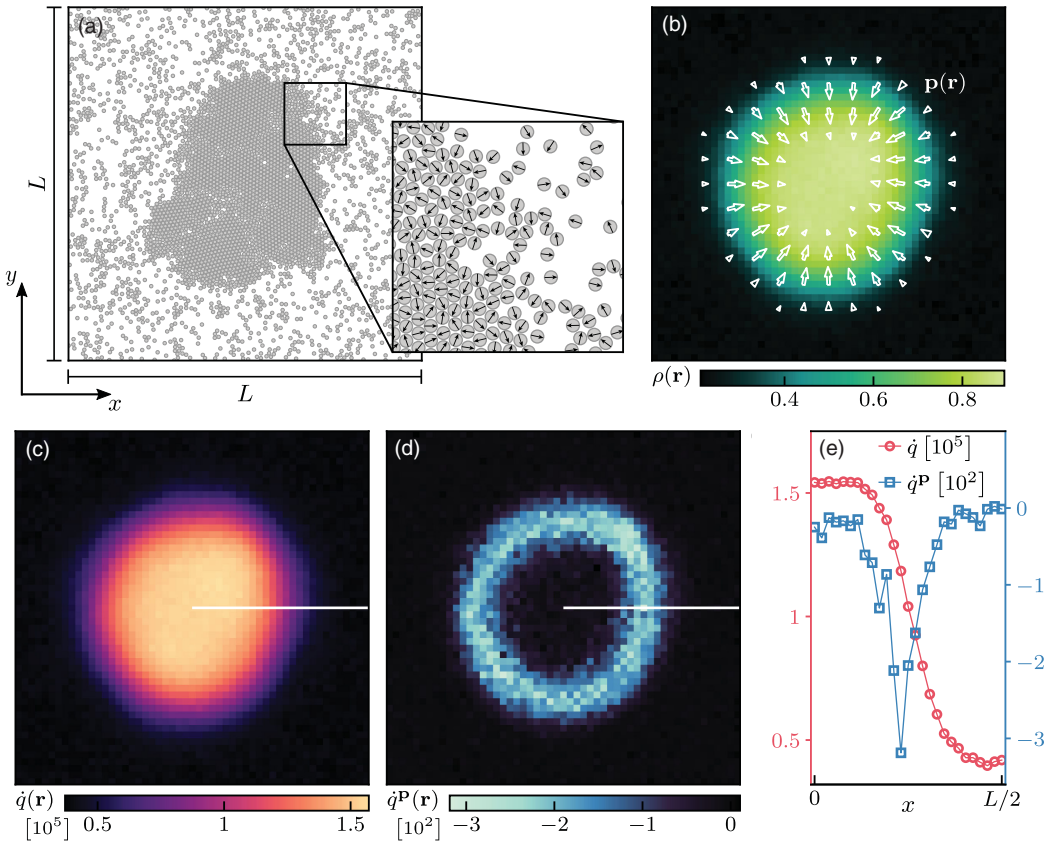

FIG. 6. Suspension of active Brownian particles undergoing MIPS. (a) Simulation snapshot showing the coexistence of a dense liquid cluster surrounded by a gaseous background in an $L \times L$ square [for details, see Appendix F 2]. The inset shows an enlargement of the marked region, where arrows indicate individual particle orientations. (b) Density field $\rho(\mathbf{r})$ (colors) and polarization field $\mathbf{p}(\mathbf{r})$ (arrows), obtained by averaging over binned simulation data. Arrow sizes indicate the polarization magnitude. (c) Local dissipation rate $\dot{q}(\mathbf{r})$ calculated according to Eq. (41) and (d) the dissipation rate without density-dependent source terms, $\dot{q}^{\mathbf{p}} = \dot{q} - v_0 \Delta\mu\rho/\lambda$, using the fields depicted in (b). (e) Profiles of local (circles) and residual (squares) dissipation rates, showing a cross section of the system as indicated by the white lines in (c) and (d). Lines connecting markers are a guide to the eye. Here, we use parameter values $v_0 = 80$ and $\lambda = 10^{-3}$ and fix the product $k_{\mathrm{eff}}\lambda = 50$.

taking negative values only [see Figs. 6(d) and 6(e)]. Hence, the interplay between local polar order and interactions *reduces* the amount of work required to maintain the nonequilibrium phase separation. Such a reduction is in agreement with the intuition provided through the local detailed balance condition: Going up in potential energy (toward denser regions) lowers the conversion rate and, consequently, the chemical current and local dissipation rate. Note that this correction is orders of magnitude smaller than the dominant contribution $v_0\Delta\mu\rho/\lambda$ [cf. Figs. 6(c)–6(e)]. In the linear response regime, a qualitatively similar behavior was observed following a phenomenological top-down approach [146] that, however, potentially suffers from a gauge freedom that cannot be resolved without knowledge of microscopic details (see Sec. V B).

In the gaseous phase, interaction forces and polarization density are negligibly small, and dissipation is decided by the corresponding bulk density alone. As a result, the work extracted from the chemostat reduces drastically and converges to a nonzero bulk value, preserving particle motility and keeping the system out of (local) equilibrium.

Complementary studies concerning the informatic entropy production of a scalar active field theory undergoing MIPS (active model B [49]), in contrast, report a strongly peaked irreversibility measure at the liquid-gas interface and small constant values within the bulk phases [106]. This should come as no surprise, since path entropy accounts for only the irreversibility encoded in the effective model dynamics, which manifests through density gradients at the interface and is agnostic to the energy dissipated by the underlying self-propulsion mechanism. As already recognized, disregarding these degrees of freedom renders their description thermodynamically inconsistent and incompatible with the notions of stochastic thermodynamics [4,118]. Therefore, even in the dense region where heat dissipation and, consequently, the distance to a state of thermal equilibrium is greatest, it returns only minimal values. By subtracting the density-dependent source term entering Eq. (41), our local dissipation rate shows similar characteristics [see Figs. 6(d) and 6(e)]. Crucially, however, although maintenance of the interface between coexisting phases is stimulated by the nonequilibrium nature of the dynamics, dissipation itself is reduced due to the polar order. Hence, knowledge of the heat dissipation in active systems (and by association the *thermodynamic* entropy production) requires the rigorous bookkeeping of the partaking degrees of freedom and cannot be inferred solely from the resulting effective model dynamics and its time reverse.

V. DISCUSSION

A. Tight coupling

Our central result is the systematic identification of the solute flux $\mathcal{J}$ [through Eqs. (31) and (39)] between the two reservoirs that is mediated by the active particles. This flux is tightly coupled to the particle speeds due to the fact that each chemical event is necessarily accompanied by an active translation of the particle. One might, thus, wonder how much of this flux could have been inferred from the evolution of particles alone, e.g., from the evolution equation (27) that depends on only a constant speed v_0 and is agnostic to the underlying mechanism that generates the propulsion speed. Within stochastic thermodynamics, there are essentially two interpretations for the term $v_0\mathbf{e}_i$: as an effective force or as an external flow field. These are distinguished by their behavior under time reversal (even vs odd). Unsurprisingly, neither interpretation yields the correct result.

For small λ after expanding to linear order, both the speeds and the solute flux [Eq. (39)] can be written as two contributions. The first contribution depends on only the constant speed v_0, while the second contribution involves particle interactions through the correlations $\langle\mathbf{e}\cdot\mathbf{F}\rangle_{\mathbf{r}}$. The origin of the second contribution is the local detailed balance condition, which reduces $k^{\pm}$ if the system goes up in potential energy. The first contribution can then be interpreted as a constant "housekeeping" dissipation to keep the system away from equilibrium, which is modified by interactions. The strength of the second contribution, however, is not related to properties of the active particles but to the underlying propulsion mechanism and the solvent through $D^{\mathrm{c}} = k_{\mathrm{eff}}\lambda^2$. Recall that k_{eff} depends on the total concentration of solute molecules [Eq. (4)]. In equilibrium ($v_0 = 0$ and $\mathbf{f}^{\mathrm{ex}} = 0$), the solute flux vanishes $\mathcal{J} = 0$, since $\langle\mathbf{e}\cdot\mathbf{F}\rangle_{\mathbf{r}} = 0$ and $\mathbf{p} = 0$.

In the linear response regime, i.e., if the system operates close to thermal equilibrium ($\beta\Delta\mu \ll 1$), the self-propulsion speed reduces to

$$v_0 = k_{\mathrm{eff}}\lambda\beta\Delta\mu. \tag{44}$$

The bulk dissipation rate on the mesoscale [Eq. (31)] to linear order in $\Delta\mu$ (and in the absence of external forces) reads

$$\dot{Q}^{\mathrm{lin}} = \sum_{i=1}^{N}\int \mathrm{d}\mathbf{r}^N\mathrm{d}\mathbf{e}^N\left[\frac{v_0^2}{\mu^{\mathrm{c}}} - v_0\mathbf{e}_i\cdot(\nabla_i U)\right]\psi \tag{45}$$

when expressed as a function of the propulsion speed v_0. This result has been obtained previously by Pietzonka and Seifert for the dissipation rate of catalytic particles through examining the continuum limit of a lattice model [138]. The fact that it recovers the dissipation only to linear order in $\Delta\mu$ is caused by taking the lattice constant to zero when coarse-graining the dynamics to a continuous state space. We emphasize that in deriving Eq. (31), and, therefore, also the macroscopic dissipation rate [Eq. (37)], no such assumption is made, and it holds arbitrarily far from equilibrium.

B. Linear irreversible thermodynamics

The linear response regime close to thermal equilibrium ($\Delta\mu = 0$) is of particular interest, since the dissipation rate should follow from more generic arguments that are agnostic toward microscopic details. The framework of linear irreversible thermodynamics requires the identification of driving affinities and their conjugate macroscopic currents which describe the exchange between system and reservoirs [58–60]. This framework has been applied to active matter systems [137,140,141,146,150]. A major advantage of our bottom-up approach is that we can now demonstrate how such a framework unfolds.

In what follows, we consider the macroscopic thermodynamic affinities $\beta\Delta\mu$ and constant $\beta\mathbf{F}^{\mathrm{ex}} = \beta\mathbf{f}^{\mathrm{ex}}$ as small perturbations away from thermal equilibrium. As a first step, we seek closed expressions, to linear order in the affinities, for the force average $\langle\mathbf{F}\rangle_{\mathbf{r}}$ and the interaction-orientation correlation function $\langle\mathbf{e}\cdot\mathbf{F}\rangle_{\mathbf{r}}$ that appear in Eqs. (35) and (38), respectively. An explicit linear response calculation yields (for details, see Appendix E 1)

$$\langle\mathbf{F}\rangle_{\mathbf{r}} = \langle\mathbf{F}\rangle_{\mathbf{r}}^{\mathrm{eq}} \quad \text{and} \quad \langle\mathbf{e}\cdot\mathbf{F}\rangle_{\mathbf{r}} = 0. \tag{46}$$

Here, we denote averages with respect to the equilibrium distribution $\psi^{\mathrm{eq}} \sim e^{-\beta U}$ as $\langle\cdot\rangle^{\mathrm{eq}}$ and use the facts that in equilibrium (i) force averages vanish and (ii) $\langle\mathbf{e}\cdot\mathbf{F}\rangle_{\mathbf{r}}^{\mathrm{eq}} = 0$ since orientations and interactions decorrelate. Remarkably, pair interactions completely decouple from thermodynamic affinities at linear order. Moreover, in homogeneous equilibrium states, the interaction contributions vanish all together.

By inserting Eq. (44) and collecting terms, one can express the coupling between particle current [Eq. (35)] and chemical current [Eq. (38)] via a symmetric Onsager matrix

$$\begin{pmatrix}\mathbf{j}\\ j^{\mathrm{c}}\end{pmatrix} = \begin{pmatrix} D_0\rho\mathbf{1} & k_{\mathrm{eff}}\lambda\mathbf{p}\\ k_{\mathrm{eff}}\lambda\mathbf{p}^{\mathsf{T}} & k_{\mathrm{eff}}\rho\end{pmatrix}\begin{pmatrix}\beta\mathbf{f}^{\mathrm{ex}}\\ \beta\Delta\mu\end{pmatrix}. \tag{47}$$

Because of the hydrostatic equilibrium condition $\nabla\cdot\boldsymbol{\sigma} = 0$, the stress term entering Eq. (35) vanishes for perturbations up to linear order in the affinities. We emphasize that we make no assumption that restricts the applicability of Eq. (47) to homogeneous states, since $\boldsymbol{\sigma}$ can be arbitrarily large and, in particular, nonuniform. Polarization fields appearing in Eq. (47) have been included to demonstrate the symmetry of the Onsager matrix but should be evaluated in equilibrium and, consequently, vanish. Similarly, the $\nabla\cdot\mathbf{p}$ term that appears in Eq. (38) vanishes to linear order. Thus, particle and chemical currents completely decouple for linear perturbations around thermal equilibrium. This no longer applies for linear perturbations around *nonequilibrium stationary states*. As we show in Appendix E 2, the coupling between affinities and currents is akin to Eq. (47) but with now nonzero and no longer symmetric off-diagonal elements. Furthermore, both currents attain an additional housekeeping contribution necessary to maintain the nonequilibrium dynamics.

Within linear irreversible thermodynamics [58], the local dissipation rate follows as the sum of products between linear Onsager currents [left-hand side in Eq. (47)] and the associated generalized forces $\{\beta\mathbf{f}^{\mathrm{ex}}, \beta\Delta\mu\}$:

$$\dot{q}^{\mathrm{lin}} = j^{\mathrm{c}}\Delta\mu + \mathbf{j}\cdot\mathbf{f}^{\mathrm{ex}}. \tag{48}$$

In agreement with the argument presented in Sec. III C 2 and the resulting identification of the local dissipation rate in Eq. (41), we find that boundary terms due to conservative forces do not influence the local dissipation rate in the linear response regime. Likewise, upon averaging in space, the total dissipation rate of the system is given by

$$\dot{Q}^{\mathrm{lin}} = \int \mathrm{d}\mathbf{r}\left(\frac{v_0^2}{\mu^{\mathrm{c}}} + \mu_0|\mathbf{f}^{\mathrm{ex}}|^2\right)\rho \tag{49}$$

and, accordingly, solely determined by bulk contributions from chemical events and the nonconservative external drive. Additionally, since interactions and orientations are uncorrelated at linear order, the only nonzero chemical contribution stems from the continual dissipation that is necessary to maintain directed motion. We have, thus, shown that naive application of the phenomenological theory of linear irreversible thermodynamics recovers expressions for the local and global dissipation rate that agree with the results obtained via explicit coarse-graining in Sec. III C 2.

Employing a top-down approach, Refs. [124,146] expand particle and chemical current

$$\begin{pmatrix}\mathbf{j}\\ j^{\mathrm{c}}\end{pmatrix} = \mathbf{L}\begin{pmatrix}-\nabla\chi\\ \Delta\mu\end{pmatrix} \tag{50}$$

with symmetric (but otherwise undetermined) matrix $\mathbf{L}$ and scalar field $\chi(\mathbf{r})$ that takes the role of a nonuniform chemical potential. The local dissipation rate

$$\dot{q}_{\mathrm{TD}}^{\mathrm{lin}} = j^{\mathrm{c}}\Delta\mu - \mathbf{j}\cdot\nabla\chi \tag{51}$$

following from the sum of products of currents and affinities now includes a boundary term $\nabla\cdot\mathbf{J}$ with $\mathbf{J} = -\mathbf{j}\chi$. As discussed in Sec. III C 2, this term arises from conservative forces and needs to be absent to render the local dissipation rate unambiguous. In future work, we will explore how collective forces, such as those arising from a nonuniform chemical potential, can be included in our systematic coarse-graining procedure.

C. Scalar field theory

Before concluding, we briefly sketch what dissipation can be inferred when going the final step to a scalar field theory through (adiabatically) eliminating the polarization field and all higher moments. To do so, we consider the

limit of large length scales and timescales that are considerably longer than the characteristic decay time of orientational moments D_r^{-1} [53,175]. Moreover, we set $\mathbf{F}^{ex} = 0$ and employ a force closure to the conditional force to truncate the hierarchy [53]. The latter allows us to rewrite Eq. (33) as $\mathbf{F} = -\zeta\rho\mathbf{e}$, where the coefficient ζ depends on the pair potential $u(r)$ and the pair distribution $g(\mathbf{r}' - \mathbf{r}|\mathbf{e}) = \psi_2/\rho$. With these assumptions, we solve Eq. (36) for the polarization field

$$\mathbf{p}^{ad} \approx -\frac{v_0 - 2\mu_0\zeta\rho}{2D_r}\nabla\rho, \tag{52}$$

which, thus, adiabatically follows changes of the particle density. The local density is the sole scalar order parameter of the theory.

Plugging Eq. (52) together with $\langle \mathbf{e}\cdot\mathbf{F}\rangle = -\zeta\rho$ for the correlations into the expression of the local dissipated heat rate [Eq. (41)], we find

$$\dot{q}^{ad}(\mathbf{r}) = \Delta\mu\left[\frac{v_0}{\lambda}\rho - \zeta\frac{\mu^c}{\lambda}\left(\rho^2 + \frac{D_0}{2D_r}\nabla^2\rho^2\right)\right] \tag{53}$$

to linear order in λ. The first term again captures the incessant energy consumption required to drive the directed motion and to keep the system from reaching thermal equilibrium. In contrast to the general result in Eq. (41), the second term suggests a density (and spatial derivatives thereof) -dependent reduction of dissipation in the adiabatic approximation. Hence, in this simplest of cases, divergence of the polarization is substituted by a term of the order of $\mathcal{O}(\rho^2, \nabla^2)$, and the orientation-interaction correlation function simply reduces to the squared local density.

While higher-order expansion schemes have recently been shown to recover the popular extensions of classical model B [176], termed active model B(+) [49,50], a universally agreed upon recipe to derive microscopically informed effective field parameters is still an open challenge [55,57,177]. Nevertheless, as illustrated above, once connections between hydrodynamic fields and a single scalar order parameter are established, one can readily apply the derived expressions for the dissipation rate [Eqs. (37) and (41)] to unravel thermodynamic details of the system at hand.

VI. CONCLUSIONS

Over the past decade, active matter has emerged as a central paradigm for self-organization in soft and living matter and has become a pillar of modern-day statistical physics. Concerned with the effects of local dissipation of residual or stored free energy and its ramifications on the (dynamical) behavior of individual or large collectives of motile entities, active matter systems are by construction out of thermal equilibrium. This makes predicting physical properties a challenging endeavor, prompting immense efforts from experimentalists and theoreticians alike. Many models are inspired by biological systems, ranging from motile bacteria such as *Escherichia coli* [178,179] to complex cellular reorganization during mitosis [12,180]. Any inquiry about the energetic cost to sustain cellular processes demands an accurate thermodynamic theory for active matter. One promising basis to build upon is the framework of stochastic thermodynamics, which extends notions of classical thermodynamics to microscopic systems governed by fluctuations. The use of stochastic thermodynamics requires the modeling of *all* degrees of freedom contributing to the dissipation, and the few *consistent* applications to active matter are usually restricted to single agents or the linear response regime [137–143].

We have achieved the next step toward a thermodynamically consistent theory for active matter by deriving the exact heat dissipation rate of catalytically propelled colloidal particles, thereby bridging the gap between individual micron-sized particles and macroscopic collectives (Fig. 1). By employing a systematic bottom-up approach, we have established connections between a microscopic model of a catalytic particle with explicit solute degrees of freedom, mesoscopic active Brownian particles, and macroscopic field theories. On the microscale, we have analytically shown how surface-mediated catalysis of molecular solutes leads to self-propulsion, without resorting to hydrodynamics. We derived the functional forms of the solute flux [Eq. (3)] and the forces that fuel molecules exert on the colloidal particle [Eq. (2)] and showed that the former defines the particle self-propulsion speed together with an effective jump length λ [Eq. (5)]. To validate the theoretical prediction, we further performed Brownian dynamics simulations of a three-dimensional catalyst surrounded by explicit solute molecules. All results for the explicit model are faithfully reproduced by an effective model that tightly couples chemical events and particle translation. Introducing interactions between active particles, we arrived at a thermodynamically consistent many-body model that reduces to the well-known model of active Brownian particles [Eq. (27)] in the (physically motivated) limit of small jump length λ. We complement this model with the *exact* expression for the dissipation [Eq. (31)]. Even in the limit where the large-scale behavior is governed through the speed v_0 as the relevant parameter, the dissipated heat depends on microscopic details, which in our model are condensed into the jump length λ and the attempt rate k_{eff}. From there, we took the final step to coupled hydrodynamic equations for the evolution of (smooth) density and polarization fields. We note that our results extend to diffusiophoretic colloidal particles that are driven through the demixing of a binary solute [135].

The main benefit of our systematic bottom-up construction is that local thermodynamic information is preserved through every coarse-graining step, ultimately yielding exact expressions at the macroscale. Here, we have focused

on the dissipation and reported how tracking of the stochastic energetics allows the systematic identification of the solute flux $\mathcal{J}$ between chemical reservoirs at each level. On the level of hydrodynamic fields, there is an apparent gauge freedom: Adding a term $\nabla \cdot \mathbf{J}$ to the local dissipation rate $\dot{q}$ does not change the global average dissipation. Considering the exchange between (virtual) subsystems, our bottom-up approach allows us to resolve this issue, and we have explored consequence for the linear response regime.

Beyond linear response, our results open new avenues to the design of active engines that exploit nonequilibrium fluctuations to extract work, by unveiling all mechanisms that constitute dissipation and the influence of external confinement. Moreover, our general insights enable strategies to infer dissipation from observable large-scale data in a wide range of systems. For example, lower bounds to the actual dissipation provide valuable insights into living systems [76,86,181–183] but typically capture only a fraction of the actual dissipation. The identification of tightly coupled degrees of freedom offers a new perspective on these systems.

ACKNOWLEDGMENTS

We thank Sebastian Bauer for preliminary results on the explicit model (Sec. II) and Ashreya Jayaram for code and data (Sec. IV B). We acknowledge financial support by the Deutsche Forschungsgemeinschaft (DFG) through the collaborative research centers TRR 146 (Grant No. 233630050) and SFB 1551 (Grant No. 464588647). J. F. R. gratefully acknowledges financial support from the Alexander von Humboldt foundation.

APPENDIX A: EXPLICIT MODEL

1. Thin interaction layer approximation

Here, we provide details for the calculation of the distribution of solute molecules around a single catalytic colloidal particle [cf. Fig. 2(a)] and how this distribution determines fluxes and the force. To this end, we assume that there is a thin layer of width ℓ on the surface of the colloidal particle within which the densities of solutes quickly drop to zero as r is decreased (cf. Fig. 7). In this appendix, we implicitly work in dimensionless quantities: length $\mathbf{r} \to \ell \mathbf{r}$, time $t \to k_0^{-1} t$ with rates $k^{\pm}(r,\theta) \to k_0 h(\theta) k^{\pm}(r)$, and energies $u_\alpha \to k_B T u_\alpha$. In steady state, the scaled current densities then obey

$$\nabla \cdot \hat{\mathbf{j}}_\alpha = \begin{cases} 0 & (r > r_C) \\ \varepsilon h(\theta) K_{\alpha\alpha'} c_{\alpha'} & (r < r_C) \end{cases} \tag{A1}$$

with $\hat{\mathbf{j}}_\alpha(r,\theta) \equiv -u'_\alpha(r) c_\alpha \hat{\mathbf{e}}_r - \nabla c_\alpha$, and we define the small parameter $\varepsilon \equiv \ell^2 k_0 / D \ll 1$. In this section, we sum over repeated indices (summation convention). Continuity at $r = r_C$ is enforced by appropriate selection of coefficients.

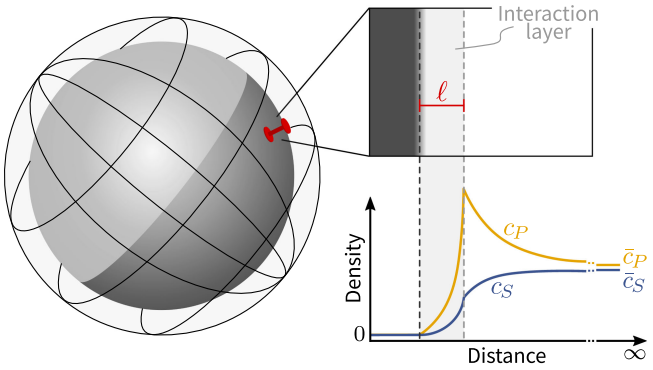

FIG. 7. Schematic illustration of the thin-layer approximation. Within the shaded interaction layer of width ℓ (scale is exaggerated for illustrative purpose) solute densities quickly decay to zero.

Note that here we neglect the diffusion of the catalytic particle (since $D_0 \ll D$). The rate matrix reads

$$\mathbf{K}(r) = \begin{pmatrix} K_{SS} & K_{SP} \\ K_{PS} & K_{PP} \end{pmatrix} = \begin{pmatrix} -k^+ & k^- \\ k^+ & -k^- \end{pmatrix}, \tag{A2}$$

and $h(\theta)$ is an indicator function that is unity on active and zero on inert regions.

We expand the solute densities

$$c_\alpha(r,\theta) = \sum_{l=0}^{\infty} a_{\alpha,l}(r) P_l(\cos\theta) \tag{A3}$$

in terms of Legendre polynomials $P_l(x)$ with coefficients $a_{\alpha,l}(r)$. For $\varepsilon = 0$, the full solution is the isotropic profile

$$c_\alpha^{(0)}(r) = a_{\alpha,0}^{(0)}(r) = \bar{c}_\alpha e^{-u_\alpha(r)}, \qquad a_{\alpha,l>0}^{(0)} = 0 \tag{A4}$$

with constant densities $\bar{c}_\alpha$ outside the interaction range, which are determined by the chemostat. Note that Eq. (A4) is simply the equilibrium profile of an ideal gas in an external field (i.e., the barometric law). In the free region $r > r_C$ (superscript $>$) with boundary conditions $c_\alpha(r \to \infty) = \bar{c}_\alpha$, we have $a_{\alpha,l}^{>}(r) = \bar{c}_\alpha \delta_{l0} + b_{\alpha,l} r^{-(l+1)}$ with constant coefficients $b_{\alpha,l}$.

Within the interaction region ($r < r_C$), we expand $c_\alpha = c_\alpha^{(0)} + \varepsilon c_\alpha^{(1)} + \mathcal{O}(\varepsilon^2)$. Projecting Eq. (A1) on the lth Legendre polynomial within a sphere of radius r leads to

$$\frac{2l+1}{2} \int_{|\mathbf{r}|<r} \mathrm{d}^3\mathbf{r}\, P_l(\cos\theta) \nabla \cdot \hat{\mathbf{j}}_\alpha^{(1)} = h_l I_\alpha(r) \tag{A5}$$

with coefficients

$$h_l \equiv \frac{2l+1}{2} \int_0^\pi \mathrm{d}\theta \sin\theta h(\theta) P_l(\cos\theta), \tag{A6}$$

giving $h_0 = 1/2$ and $h_1 = 3/4$, and integral

$$I_\alpha(r) \equiv 2\pi \int_0^r \mathrm{d}\xi\, \xi^2 \sum_{\alpha'} K_{\alpha\alpha'}(\xi)\bar{c}_{\alpha'} e^{-u_{\alpha'}(\xi)} = -2\pi(\bar{c}_S - \bar{c}_P)\int_0^r \mathrm{d}\xi\, \xi^2 k_\alpha(\xi) e^{-u_\alpha(\xi)} \quad \text{(A7)}$$

involving the zero-order solution $c_\alpha^{(0)}$. The second line is obtained through utilizing the detailed balance condition [Eq. (1)], defining $k_S \equiv k^+$ and $k_P \equiv -k^-$ along the way. Because of the shape of the rate matrix [Eq. (A2)], we immediately see that $I_S = -I_P$, which is a consequence of mass conservation.

To rewrite Eq. (A5), we exploit $P_l \nabla \cdot \hat{\mathbf{j}}_\alpha = \nabla \cdot (P_l \hat{\mathbf{j}}_\alpha) - \hat{\mathbf{j}}_\alpha \cdot \nabla P_l$ together with the divergence theorem for the first term to obtain the integro-differential equation

$$-2\pi r^2 \left\{ u'_\alpha(r) a^{(1)}_{\alpha,l}(r) + \left[a^{(1)}_{\alpha,l}(r) \right]' \right\} + 2\pi \sum_{k=0}^{\infty} \int_0^r \mathrm{d}\xi\, M_{lk} a^{(1)}_{\alpha,k}(\xi) = h_l I_\alpha(r) \quad \text{(A8)}$$

for the coefficients $a^{(1)}_{\alpha,l}$. We have defined

$$M_{lk} \equiv \frac{2l+1}{2}\int_{-1}^{1} \mathrm{d}x (1-x^2) P'_k(x) P'_l(x) = l(l+1)\delta_{lk}, \quad \text{(A9)}$$

with the final expression following after integrating by parts and using Legendre's differential equation.

2. Solute flux

The first quantity we are interested in is the flux between the reservoirs. Plugging the series Eq. (A3) into the expression

$$J_\alpha(r) = 2\pi r^2 \varepsilon^{-1} \int_0^\pi \mathrm{d}\theta \sin\theta \hat{\mathbf{e}}_r \cdot \hat{\mathbf{j}}_\alpha = -4\pi r^2 \varepsilon^{-1} [u'_\alpha(r) a_{\alpha,0}(r) + a'_{\alpha,0}(r)] \quad \text{(A10)}$$

for the flux of molecular solutes through a spherical surface with radius r leads to an expression that depends only on the $l = 0$ coefficient $a_{\alpha,0}(r)$. In the free region, $J^>_\alpha = 4\pi\varepsilon^{-1} b_{\alpha,0}$ is manifestly independent of r. Inside the interaction range, we see that the square brackets in Eq. (A10) are zero for $a^{(0)}_{\alpha,0} = c^{(0)}_\alpha$, and we use Eq. (A8) to obtain $J^{(1)}_\alpha(r) = 2h_0 I_\alpha(r)$ at the next order. Since $I_S = -I_P$, we find $J_S(r) + J_P(r) = 0$ everywhere, which guarantees the conservation of the total number of molecular solutes. The difference

$$\mathcal{J} \equiv J^{(1)}_P(r_\mathrm{C}) - J^{(1)}_S(r_\mathrm{C}) = 4h_0 I_P(r_\mathrm{C}) \quad \text{(A11)}$$

is the net flux from the substrate reservoir to the product reservoir. Inserting $h_0 = 1/2$ and Eq. (A7) into this expression gives Eqs. (3) and (4) in the main text.

3. Force

For the propulsion speed, we need the forces exerted by the solute molecules on the colloidal particle, which read

$$\mathbf{g}_\alpha = \int_0^{r_\mathrm{C}} \mathrm{d}r\, r^2 \int_0^\pi \mathrm{d}\theta \sin\theta \int_0^{2\pi} \mathrm{d}\varphi [u'_\alpha(r)\hat{\mathbf{e}}_r] c_\alpha(r,\theta) = \frac{4\pi}{3}\int_0^{r_\mathrm{C}} \mathrm{d}r\, r^2 u'_\alpha(r) a_{\alpha,1}(r)\hat{\mathbf{e}}_z \quad \text{(A12)}$$

with total force $\mathbf{g} = \mathbf{g}_S + \mathbf{g}_P$. The force, thus, requires knowledge of the function $a^{(1)}_{\alpha,1}(r)$. Taking the derivative of Eq. (A8) with respect to r, dividing by $2\pi r^2$, and writing $a^{(1)}_{\alpha,1} = \chi_\alpha e^{-u_\alpha}$ leads to the linear differential equation

$$\nabla^2 \chi_\alpha - \frac{2}{r^2}\chi_\alpha - u'_\alpha \chi'_\alpha = h_1(\bar{c}_S - \bar{c}_P) k_\alpha \quad \text{(A13)}$$

for $\chi_\alpha(r)$. Since the homogeneous solution has to be zero [cf. Eq. (A4)], we are interested in only the particular solution $\chi_\alpha(r) = h_1(\bar{c}_S - \bar{c}_P)\int \mathrm{d}\boldsymbol{\xi}\, G_\alpha(|\mathbf{r} - \boldsymbol{\xi}|) k_\alpha(\boldsymbol{\xi})$. The (unknown) Green's function $G_\alpha(r)$ depends on the pair potential $u_\alpha(r)$. Inserting this solution into Eq. (A12) and restoring dimensionful quantities leads to the force given in Eq. (2) in the main text, with a functional

$$\mathcal{V} \equiv \frac{4\pi}{3}\sum_\alpha \int_0^{r_\mathrm{C}} \mathrm{d}r\, r^2 u'_\alpha e^{-u'_\alpha} \int \mathrm{d}\boldsymbol{\xi} G_\alpha(|\mathbf{r} - \boldsymbol{\xi}|) k_\alpha(\boldsymbol{\xi}) \quad \text{(A14)}$$

that encodes the microscopic solute-colloid interactions but is independent of the chemostat.

APPENDIX B: CHOICE OF TRANSITION RATES

In contrast to the exponential rates in Eq. (24), prevalently used in the field of stochastic thermodynamics, we briefly show that one could have similarly employed an ansatz based on the Glauber rates in Eq. (7). Following a straightforward generalization suggests rates of the form

$$k_i^\pm = k_\mathrm{eff}\left[1 + e^{\mp\beta\Delta\mu} e^{-\beta[-U(\mathbf{r}_i \pm \lambda\mathbf{e}_i) + U(\mathbf{r}_i) \pm \lambda \mathbf{e}_i \cdot \mathbf{F}_i^\mathrm{ex}]}\right]^{-1}. \quad \text{(B1)}$$

Clearly, local detailed balance is satisfied [cf. Eq. (20)] and, consequently, thermodynamic consistency guaranteed. After an expansion to linear order of small displacement length λ, we obtain

$$k_i^\pm = \tilde{\kappa}^\pm \left[1 \pm \frac{\lambda\beta}{e^{\pm\beta\Delta\mu} + 1}\mathbf{e}_i \cdot (\mathbf{F}_i^\mathrm{ex} - \nabla_i U)\right] + \mathcal{O}(\lambda^2), \quad \text{(B2)}$$

with $\tilde{\kappa}^{\pm} \equiv k_{\mathrm{eff}}(1+e^{\mp\beta\Delta\mu})^{-1}$. Plugging this expansion, alongside Eqs. (C1) and (C2), into Eq. (14), we recover an equation of motion identical to the one written in Eq. (27) by defining

$$v_0 \equiv \lambda(\tilde{\kappa}^{+} - \tilde{\kappa}^{-}) \tag{B3}$$

and

$$\mu^{\mathrm{c}} \equiv \lambda^2\beta\frac{2e^{\beta\Delta\mu}}{(e^{\beta\Delta\mu}+1)^2}, \tag{B4}$$

as the corresponding speed and chemical mobility, respectively.

Lastly, in the linear response regime, assuming $\Delta\mu\beta \ll 1$, expansion to leading order results in $v_0 = k_{\mathrm{eff}}\lambda\beta\Delta\mu/2$ and $\mu^{\mathrm{c}} = k_{\mathrm{eff}}\lambda^2\beta/2$, which after renormalizing the attempt rate $k_{\mathrm{eff}} \to 2k_{\mathrm{eff}}$ recovers Eq. (44).

APPENDIX C: MESOSCOPIC MODEL

1. Expansion for small jump length

To further simplify the evolution equation of the mesoscopic model [Eq. (16)], we exploit that the microscopic jump length λ is much smaller than the size of colloidal particles (cf. Sec. II) to expand the reduced joint distribution [Eq. (23)] and transition rates [Eq. (24)]. To order λ^2, one obtains

$$\psi(\mathbf{r}_i \pm \lambda\mathbf{e}_i, \mathbf{e}_i) = \psi(\mathbf{r}_i, \mathbf{e}_i) \pm \lambda\mathbf{e}_i\cdot\nabla_i\psi(\mathbf{r}_i, \mathbf{e}_i) + \frac{\lambda^2}{2}(\mathbf{e}_i\cdot\nabla_i)^2\psi(\mathbf{r}_i, \mathbf{e}_i) + \mathcal{O}(\lambda^3) \tag{C1}$$

and

$$k_i^{\pm}(\mathbf{r}_i \mp \lambda\mathbf{e}_i) = k_i^{\pm}(\mathbf{r}_i) \mp \lambda\mathbf{e}_i\cdot\nabla_i k_i^{\pm} + \mathcal{O}(\lambda^3). \tag{C2}$$

Plugging these expansions into the definition of the discrete difference operator [Eq. (14)], we find

$$\widehat{\nabla}_i j_i^{\mathrm{c}} = \lambda\mathbf{e}_i\cdot\nabla_i\left[(k_i^{+}-k_i^{-})\psi - \frac{1}{2}\lambda(k_i^{+}+k_i^{-})\mathbf{e}_i\cdot\nabla_i\psi\right] + \mathcal{O}(\lambda^3). \tag{C3}$$

Furthermore, by employing the explicit ansatz for the transition rates made in the main text [Eq. (24)], we obtain

$$k_i^{\pm}(\mathbf{r}_i) = \kappa^{\pm}\left[1 \pm \lambda\frac{\beta}{2}\mathbf{e}_i\cdot(\mathbf{F}_i^{\mathrm{ex}} - \nabla_i U)\right] + \mathcal{O}(\lambda^2) \tag{C4}$$

to leading order in λ. Upon inserting this expansion into the discrete difference operator [Eq. (C3)], one recovers the expression given in Eq. (25), which defines the chemical current presented in Eq. (26).

a. Higher-order corrections

Throughout Sec. III, we study the model in a linear-order expansion of the small parameter λ. In this section, we briefly want to comment on higher-order corrections.

If one were to keep all terms to order λ^2 for the dynamics, the corresponding evolution equation would read from Eq. (16)

$$\frac{\partial\psi}{\partial t} = -\sum_{i=1}^{N}\{\nabla_i\cdot[v_0\mathbf{e}_i + \mu^{\mathrm{c}}(\mathbf{e}_i\mathbf{e}_i)\cdot(\mathbf{F}_i^{\mathrm{ex}} - \nabla_i U) + \mu_0(\mathbf{F}_i^{\mathrm{ex}} - \nabla_i U) - D_0\nabla_i - D^{\mathrm{c}}(\mathbf{e}_i\mathbf{e}_i)\cdot\nabla_i]\psi - D_{\mathrm{r}}\Delta_{\mathbf{e}_i}\psi\}, \tag{C5}$$

where $(\mathbf{e}_i\mathbf{e}_i)$ denotes the dyadic product of orientation vector $\mathbf{e}_i$. This closely resembles results previously obtained in Refs. [138,139,156] and captures the dynamics of ABPs, augmented by order λ^2 terms that describe how the rate of chemical events, and, consequently, the speed of particles, is influenced by their respective position, as well as how diffusion is enhanced along particle orientations. It is important to note that the chemical current enters the dynamics—in contrast to the dissipation rate [Eq. (31)]—with an additional factor of λ [cf. Eq. (25)]. Thus, truncating the expansion as done here necessarily disregards terms of the chemical current in the dynamics that, however, still appear in the dissipation rate. For example, to calculate the dissipation of the dynamics given in Eq. (C5), one would have to consider $\mathcal{O}(\lambda^2)$ corrections to the chemical current [Eq. (26)], which remain absent in the evolution equation.

b. Truncation of chemical current

Alternatively, one could truncate the chemical current [Eq. (26)] to recover expressions akin to Refs. [138,139]. In that case, j^{c} is closed, and the associated dynamical equation and dissipation rate are no longer expansions of the microscopic dynamics as introduced in Sec. II but closed expressions for a distinct microscopic model.

To highlight the subtle differences with the results in Sec. III, let us assume the chemical current [Eq. (26)] is truncated at zeroth order in λ, i.e., $j_i^{\mathrm{c}} = (v_0/\lambda)\psi \propto \mathcal{O}(1)$. By plugging j_i^{c} into Eq. (16), one obtains the evolution equation reported in Eq. (27) to linear order in λ that describes the motion of standard ABPs. The associated hydrodynamic equations are given by Eqs. (34) and (36). Upon inserting the truncated current into Eq. (31), the local dissipation rate after coarse-graining reads $\dot{q} = \Delta\mu(v_0/\lambda)\rho \propto 1$ and captures only the density-dependent housekeeping term. Here, the different order in λ is justified, since Eq. (27) and $\dot{q}$ are exact expressions for the dynamical equation and dissipation rate of the reduced model that follows from $j_i^{\mathrm{c}} \propto \mathcal{O}(1)$. Truncating j_i^{c} at $\mathcal{O}(\lambda)$, one gets Eq. (C5) for the effective dynamics and Eq. (41) for the local dissipation rate. The order of the resulting

dynamics is always increased by one when compared to the dissipation rate and truncated chemical current.

2. Bulk dissipation rate

To identify the bulk dissipation rate of the system, we rewrite the sum of chemical and particle dissipation rates [Eqs. (29) and (30)] as

$$\dot{Q} = \dot{Q}^{\mathrm{p}} + \dot{Q}^{\mathrm{c}} = \sum_{i=1}^{N} \int \mathrm{d}\mathbf{r}^N \mathrm{d}\mathbf{e}^N [j_i^{\mathrm{c}} \Delta\mu + \mathbf{j}_i \cdot (\mathbf{F}_i^{\mathrm{ex}} - \nabla_i U)], \tag{C6}$$

with $\mathbf{j}_i$ defined in Eq. (28). Exploiting the steady state condition ($\partial_t \psi = \sum_{i=1}^{N} \nabla_i \cdot \mathbf{j}_i = 0$) together with the divergence theorem and splitting the external forces into $\mathbf{F}_i^{\mathrm{ex}} = \mathbf{f}_i^{\mathrm{ex}} - \nabla_i U^{\mathrm{ex}}$, we find that contributions to the dissipation rate [Eq. (C6)] that involve conservative forces as affinity become boundary terms of the form

$$\int \mathrm{d}\mathbf{r}^N \mathrm{d}\mathbf{e}^N \mathbf{j}_i \cdot \nabla_i (U + U^{\mathrm{ex}}) = \int \mathrm{d}\mathbf{r}^{N-1} \mathrm{d}\mathbf{e}^N \int_{\partial V} \mathrm{d}\mathbf{r}_i \cdot \mathbf{j}_i (U + U^{\mathrm{ex}}). \tag{C7}$$

Note that these surface integrals vanish provided the joint distribution ψ (the particle currents $\mathbf{j}_i$) approaches zero at the system boundary ∂V. This generally holds for infinite systems and confining wall potentials. Moreover, surface terms vanish for potentials $U + U^{\mathrm{ex}}$ that are periodic and continuous across the boundary. This results in the dissipation rate reported in Eq. (31) in the main text.

In Ref. [138], the authors similarly find that conservative forces lead to (vanishing) boundary terms by multiplying the steady state evolution equation by the potential, followed by repeated integration by parts.

APPENDIX D: ACTIVE BROWNIAN PARTICLES IN THE PRESENCE OF A FLAT WALL

1. Density and polarization profiles

We provide details for the calculation of the density and polarization profiles displayed in Figs. 5(b) and 5(c). A very similar problem was previously investigated in Refs. [173,184]. We assume a two-dimensional system with an infinitely long straight wall, given by the linear potential $U^{\mathrm{ex}} = -F_0 x$ for $x < 0$. The system is translationally invariant along y, allowing us to write the steady state evolution equations for density [Eq. (34)] and polarization fields [Eq. (36)] as

$$0 = -v_0 \frac{\partial p_x}{\partial x} + D_0 \frac{\partial^2 \rho}{\partial x^2}, \tag{D1}$$

$$0 = -\frac{v_0}{2} \frac{\partial \rho}{\partial x} + D_0 \frac{\partial^2 p_x}{\partial x^2} - D_{\mathrm{r}} p_x \tag{D2}$$

in the force-free $x > 0$ region and

$$0 = -v_0 \frac{\partial p_x}{\partial x} - \mu_0 F_0 \frac{\partial \rho}{\partial x} + D_0 \frac{\partial^2 \rho}{\partial x^2}, \tag{D3}$$

$$0 = -\frac{v_0}{2} \frac{\partial \rho}{\partial x} - \mu_0 F_0 \frac{\partial p_x}{\partial x} + D_0 \frac{\partial^2 p_x}{\partial x^2} - D_{\mathrm{r}} p_x \tag{D4}$$

under the influence of a constant force F_0 if $x < 0$. Note that both ρ and p_x depend on x only. To proceed, we assume that both fields take exponential forms ($\sim e^{\alpha_\pm x}$), with inverse decay lengths $\alpha_\pm$ for the positive and negative x regions.

$x > 0$: By rearranging Eqs. (D1) and (D2), followed by insertion of the ansatz, one obtains the simple equation

$$\alpha_+^3 = \frac{1}{\xi^2} \alpha_+, \tag{D5}$$

with solutions $\alpha_+ = 0, \pm\xi^{-1}$, where we define the decay length $\xi \equiv \sqrt{D_0/D_{\mathrm{r}}}/\sqrt{1 + v_0^2/(2D_{\mathrm{r}}D_0)}$. Clearly, one can discard the positive solutions, since density and polarization must not diverge in the limit of large $x \to \infty$.

$x < 0$: Along similar lines, rewriting Eqs. (D3) and (D4) results in

$$\alpha_-^4 = 2\beta F_0 \alpha_-^3 + \left(\frac{1}{\xi^2} - \beta^2 F_0^2\right) \alpha_-^2 - \frac{D_{\mathrm{r}}}{D_0} \beta F_0 \alpha_-. \tag{D6}$$

Assuming large forces $F_0 \gg 1$, the solutions to leading order in F_0^{-1} read

$$\alpha_- = 0, \qquad -\frac{D_{\mathrm{r}}}{\beta F_0 D_0}, \qquad \beta F_0 \pm \frac{v_0}{\sqrt{2} D_0}, \tag{D7}$$

and, in analogy to above's reasoning, we can immediately discard negative solutions as well as $\alpha_- = 0$, due to the necessarily vanishing density and polarization as $x \to -\infty$.

Collecting terms, densities take the general form

$$\rho(x) = \begin{cases} C_+ e^{-x/\xi} + B & x > 0, \\ C_-^{(1)} e^{[\beta F_0 + v_0/(\sqrt{2}D_0)]x} + C_-^{(2)} e^{[\beta F_0 - v_0/(\sqrt{2}D_0)]x} & x < 0, \end{cases} \tag{D8}$$

and polarization profiles are given by

$$p_x(x) = \begin{cases} -\frac{D_0}{v_0 \xi} C_+ e^{-x/\xi} & x > 0, \\ \frac{1}{\sqrt{2}} \left(C_-^{(1)} e^{[\beta F_0 + v_0/(\sqrt{2}D_0)]x} - C_-^{(2)} e^{[\beta F_0 - v_0/(\sqrt{2}D_0)]x} \right) & x < 0. \end{cases} \tag{D9}$$

Note the necessity of sufficiently strong forces, such that $\beta F_0 > v_0/(\sqrt{2}D_0)$. The remaining four coefficients are determined by enforcing that the density converges to the bulk value ρ_b for $x \to \infty$ and that both density and polarization fields, as well as their respective currents, are continuous at $x = 0$. Under these conditions, the coefficients are given by

$$\begin{aligned} C_+ &= \frac{\rho_b v_0^2}{2D_r D_0}, \qquad B = \rho_b, \\ C_-^{(1)} &= \frac{1}{2}\left[C_+\left(1+\frac{\sqrt{2}D_0}{v_0\xi}\right)+\rho_b\right], \\ C_-^{(2)} &= \frac{1}{2}\left[C_+\left(1-\frac{\sqrt{2}D_0}{v_0\xi}\right)+\rho_b\right], \end{aligned} \tag{D10}$$

which after insertion in Eqs. (D8) and (D9) give the solutions plotted in Figs. 5(b) and 5(c) in the main text.

2. Solute flux in subdomains

With the analytical expressions for the density and polarization fields, given by Eqs. (D8) and (D9) and the associated coefficients [Eq. (D10)], we calculate the average solute fluxes $\mathcal{J}_\pm$ for the two subdomains $\Omega_\pm$, depicted in Fig. 5(a). Plugging the results into Eq. (39), we immediately find

$$\mathcal{J}_+ = L_y \int_0^{L_x} \mathrm{d}x \frac{v_0}{\lambda}\rho = \frac{v_0}{\lambda} L_y (L_x \rho_b + \xi C_+) \tag{D11}$$

for the solute flux in subregion Ω_+ and, similarly,

$$\begin{aligned} \mathcal{J}_- &= L_y \int_{-L_x}^0 \mathrm{d}x \left(\frac{v_0}{\lambda}\rho + \frac{\mu^c}{\lambda} F_0 p_x\right) \\ &= L_y \left[\frac{C_-^{(1)}(v_0 + \mu^c F_0/\sqrt{2})}{\beta F_0 + v_0/(\sqrt{2}D_0)} + \frac{C_-^{(2)}(v_0 - \mu^c F_0/\sqrt{2})}{\beta F_0 - v_0/(\sqrt{2}D_0)}\right] \end{aligned} \tag{D12}$$

for subsystem Ω_-.

APPENDIX E: LINEAR RESPONSE THEORY

1. Perturbations around equilibrium

We provide additional details on the linear response calculation preformed in Sec. V B. We start by considering the evolution equation of the joint probability distribution given in Eq. (27) and write

$$\frac{\partial \psi}{\partial t} = (\mathcal{L}^{\mathrm{eq}} + \mathcal{L}^{(1)} + \mathcal{L}^{(2)})\psi, \tag{E1}$$

with the generator of the equilibrium dynamics

$$\mathcal{L}^{\mathrm{eq}} \equiv \sum_{i=1}^N \{\nabla_i \cdot [\mu_0 \nabla_i U + D_0 \nabla_i] - D_r \Delta_{\mathbf{e}_i}\} \tag{E2}$$

and the associated generators of small perturbations

$$\mathcal{L}^{(1)} \equiv -\sum_{i=1}^N D_0 \beta \mathbf{f}^{\mathrm{ex}} \cdot \nabla_i, \tag{E3}$$

$$\mathcal{L}^{(2)} \equiv -\sum_{i=1}^N k_{\mathrm{eff}} \lambda \beta \Delta\mu \mathbf{e}_i \cdot \nabla_i. \tag{E4}$$

In the linear regime, the general solution is formally given by

$$\psi = \psi^{\mathrm{eq}} + \sum_{m\in\{1,2\}} \int_{-\infty}^t \mathrm{d}t'\, e^{\mathcal{L}^{\mathrm{eq}}(t-t')} \mathcal{L}^{(m)} \psi^{\mathrm{eq}}, \tag{E5}$$

with equilibrium distribution $\psi^{\mathrm{eq}} \sim e^{-\beta U}$, and we denote equilibrium averages as $\langle\cdot\rangle^{\mathrm{eq}}$. With the general solution [Eq. (E5)], the average of a coarse-grained observable O (introduced as a proxy for $\mathbf{F}$ and $\mathbf{e}\cdot\mathbf{F}$) takes the form

$$\begin{aligned} \langle O\rangle_{\mathbf{r}} \approx \langle O\rangle_{\mathbf{r}}^{\mathrm{eq}} + \sum_{m\in\{1,2\}} \int \mathrm{d}\mathbf{r}^N \mathrm{d}\mathbf{e}^N \int_{-\infty}^t \mathrm{d}t' \sum_{i=1}^N O_i \\ \times \delta(\mathbf{r}-\mathbf{r}_i) e^{\mathcal{L}^{\mathrm{eq}}(t-t')} \mathcal{L}^{(m)} \psi^{\mathrm{eq}}. \end{aligned} \tag{E6}$$

Here, we use the identity $\langle O\rangle_{\mathbf{r}} = \langle \sum_{i=1}^N O_i \delta(\mathbf{r}-\mathbf{r}_i)\rangle$, where $\langle\cdot\rangle$ labels the system average with respect to the perturbed distribution ψ and O_i the observable evaluated for individual particles i. By letting the generators of the small perturbations $\mathcal{L}^{(1)}$ and $\mathcal{L}^{(2)}$ act on the equilibrium distribution, we find

$$\mathcal{L}^{(1)}\psi^{\mathrm{eq}} = \sum_{i=1}^N \mu_0 \beta (\mathbf{f}^{\mathrm{ex}} \cdot \nabla_i U)\psi^{\mathrm{eq}}, \tag{E7}$$

$$\mathcal{L}^{(2)}\psi^{\mathrm{eq}} = \sum_{i=1}^N k_{\mathrm{eff}} \lambda \beta^2 \Delta\mu (\mathbf{e}_i \cdot \nabla_i U)\psi^{\mathrm{eq}}. \tag{E8}$$

Plugging these into Eq. (E6), choosing $O \in \{\mathbf{F}, \mathbf{e}\cdot\mathbf{F}\}$ and formally taking the $t \to \infty$ limit to obtain time-independent stationary expressions, the average

$$\begin{aligned} \langle \mathbf{F}\rangle_{\mathbf{r}} = \langle \mathbf{F}\rangle_{\mathbf{r}}^{\mathrm{eq}} - \mu_0 \beta \langle \mathbf{F}\rangle_{\mathbf{r}}^{\mathrm{eq}} (\langle \mathbf{F}\rangle^{\mathrm{eq}} \cdot \mathbf{f}^{\mathrm{ex}}) \\ - k_{\mathrm{eff}} \lambda \beta^2 \Delta\mu \langle \mathbf{F}\rangle_{\mathbf{r}}^{\mathrm{eq}} \langle \mathbf{e}\cdot\mathbf{F}\rangle^{\mathrm{eq}} \end{aligned} \tag{E9}$$

and orientation-interaction correlation function

$$\begin{aligned} \langle \mathbf{e}\cdot\mathbf{F}\rangle_{\mathbf{r}} = \langle \mathbf{e}\cdot\mathbf{F}\rangle_{\mathbf{r}}^{\mathrm{eq}} - \mu_0 \beta \langle \mathbf{e}\cdot\mathbf{F}\rangle_{\mathbf{r}}^{\mathrm{eq}} (\langle \mathbf{F}\rangle^{\mathrm{eq}} \cdot \mathbf{f}^{\mathrm{ex}}) \\ - k_{\mathrm{eff}} \lambda \beta^2 \Delta\mu \langle \mathbf{e}\cdot\mathbf{F}\rangle^{\mathrm{eq}} \langle \mathbf{e}\cdot\mathbf{F}\rangle_{\mathbf{r}}^{\mathrm{eq}} \end{aligned} \tag{E10}$$

are expressed through equilibrium averages and correlation functions only. Lastly, realizing that orientations and interactions are independent in equilibrium and that the equilibrated state has to (on average) be force-free, we recover the results reported in Eq. (46). In analogy, we find vanishing linear order corrections in perturbations to the density and polarization.

2. Perturbations around a nonequilibrium stationary state

To corroborate the discussion of equilibrium perturbations, we present here how nonequilibrium steady states respond to small changes $\beta\delta\Delta\mu$ in the driving affinity $\beta\Delta\mu$ that maintains the distance to thermal equilibrium and weak external perturbations through applying force $\beta\mathbf{f}^{\mathrm{ex}}$. After perturbing $\Delta\mu \to \Delta\mu + \delta\Delta\mu$, we expand the self-propulsion speed [Eq. (10)] in small $\delta\Delta\mu$ and define

$$\bar{v}_0 \equiv 2k_{\mathrm{eff}}\lambda \tanh\left(\frac{\beta\Delta\mu}{2}\right), \tag{E11}$$

$$\delta v_0 \equiv k_{\mathrm{eff}}\lambda \cosh^{-2}\left(\frac{\beta\Delta\mu}{2}\right), \tag{E12}$$

such that $v_0 \approx \bar{v}_0 + \delta v_0 \beta\delta\Delta\mu$. Analog to Eq. (E1), the Smoluchowski equation of joint distribution ψ, splits into three parts where the stationary state generator reads

$$\mathcal{L}^{\mathrm{s}} \equiv \sum_{i=1}^{N} \{\nabla_i \cdot [\mu_0 \nabla_i U + D_0 \nabla_i - \bar{v}_0 \mathbf{e}_i] - D_{\mathrm{r}} \Delta_{\mathbf{e}_i}\}, \tag{E13}$$

and perturbations are generated by operators

$$\mathcal{L}^{(1)} \equiv -\sum_{i=1}^{N} D_0 \beta \mathbf{f}^{\mathrm{ex}} \cdot \nabla_i, \tag{E14}$$

$$\mathcal{L}^{(2)} \equiv -\sum_{i=1}^{N} \delta v_0 \beta\delta\Delta\mu \mathbf{e}_i \cdot \nabla_i. \tag{E15}$$

Following the calculation presented in Appendix E 1, the average interaction force and the orientation-interaction correlation function amount to

$$\langle \mathbf{F} \rangle_{\mathbf{r}} = \langle \mathbf{F} \rangle^{\mathrm{s}}_{\mathbf{r}} \quad \text{and} \quad \langle \mathbf{e} \cdot \mathbf{F} \rangle_{\mathbf{r}} = \langle \mathbf{e} \cdot \mathbf{F} \rangle^{\mathrm{s}}_{\mathbf{r}}, \tag{E16}$$

since terms linear in the affinities cancel. Here, we denote averages with respect to the (generally unknown) stationary measure ψ^{s} as $\langle\cdot\rangle^{\mathrm{s}}$. Plugging these results in the expressions for the particle and chemical current, given by Eqs. (35) and (38), respectively, yields

$$\begin{pmatrix} \mathbf{j} - \mu_0 \nabla \cdot \boldsymbol{\sigma}^{\mathrm{s}} \\ j^{\mathrm{c}} + k_{\mathrm{eff}}\lambda(\nabla \cdot \mathbf{p} - \beta \langle \mathbf{e} \cdot \mathbf{F} \rangle^{\mathrm{s}}_{\mathbf{r}}) \end{pmatrix} = \begin{pmatrix} \bar{v}_0 \mathbf{p} \\ \bar{v}_0 \rho/\lambda \end{pmatrix} + \begin{pmatrix} D_0 \rho \mathbf{1} & \delta v_0 \mathbf{p} \\ k_{\mathrm{eff}}\lambda \mathbf{p}^{\intercal} & \delta v_0 \rho/\lambda \end{pmatrix} \begin{pmatrix} \beta \mathbf{f}^{\mathrm{ex}} \\ \beta\delta\Delta\mu \end{pmatrix} \tag{E17}$$

with stress tensor $\boldsymbol{\sigma}^{\mathrm{s}} = -k_{\mathrm{B}}T\rho\mathbf{1} + \boldsymbol{\sigma}^{\mathrm{s}}_{\mathrm{IK}}$ and $\nabla \cdot \boldsymbol{\sigma}^{\mathrm{s}}_{\mathrm{IK}} = \langle \mathbf{F} \rangle^{\mathrm{s}}_{\mathbf{r}}$. Notably, both the particle and chemical current attain an additional term that captures the incessant conversion of substrate molecules, required for housekeeping of the nonequilibrium steady state (first term on the right-hand side). Moreover, both currents acquire additional kinetic contributions due to the nonvanishing correlation function between orientations and interactions, the generally nonzero stress, and possible polar order.

APPENDIX F: SIMULATION DETAILS

1. Explicit model

We simulate an $L \times L \times L$ box with $L = 8r_{\mathrm{C}}$, where r_{C} is the radius of the catalyst at the origin. We model the solute-catalyst interactions as excluded volume via the repulsive short-ranged Weeks-Chandler-Anderson potential

$$u(r;\epsilon,\sigma) = \begin{cases} 4\epsilon\left[\left(\frac{\sigma}{r}\right)^{12} - \left(\frac{\sigma}{r}\right)^{6}\right] + \epsilon & \text{if } r < 2^{1/6}\sigma, \\ 0 & \text{otherwise} \end{cases} \tag{F1}$$

with $u_\alpha(r) \equiv u(r;\epsilon_\alpha, r_{\mathrm{C}})$. We employ $\epsilon_S = 10$ for substrate and $\epsilon_P = 1$ for product solutes. Inside the catalytic zone, we attempt a chemical event with probability $p_0 = 0.1$ each time step, fixing an attempt rate $k_0 = p_0/\delta t$, where $\delta t = 10^{-4}$ is the discretization of time (in Brownian units) for integration of the translational degrees of freedom.

The repulsive potential of the catalyst shifts the equilibrium concentrations by decreasing the effective system volume. The solute molecule population is consequently asymmetric even in a state of thermal equilibrium $[N_S^{\mathrm{eq}} \neq N_P^{\mathrm{eq}} \neq (N_S + N_P)/2]$ and shifts the chemical potential difference by the (logarithm of) equilibrium constant $K = N_S^{\mathrm{eq}}/N_P^{\mathrm{eq}}$. From the partition function

$$Z(N_S, N_P) = \frac{\nu_S^{N_S} \nu_P^{N_P}}{\lambda_T^{3(N_S+N_P)} N_S! N_P!}, \tag{F2}$$

with thermal de Broglie wavelength λ_T and effective volumes

$$\nu_\alpha \equiv V + 4\pi \int_0^{r_{\mathrm{C}}} \mathrm{d}r\, r^2 (e^{-\beta u_\alpha(r)} - 1), \tag{F3}$$

we find $K = \nu_S/\nu_P$ upon setting the chemical potentials equal. For small packing fractions of catalytic particles, i.e., large system volume V, their effect on the equilibrium population is negligible as $K \to 1$, leaving equal fractions

of substrate and product molecules. The constant K introduces an effective ideal contribution to the chemical potential, that we inserted into Eq. (6) in the main text in order to use the relative concentrations in the reservoir $\Delta\mu = \ln \bar{c}_S/\bar{c}_P$ as the control parameter for activity.

2. Active Brownian particles

To investigate the dissipation rate of particles undergoing MIPS, we simulate a suspension of $N = 4000$ active particles of diameter σ in a rectangular $L \times L$ box, with edge length $L \approx 102.3$ and periodic boundary conditions. The global packing fraction is $\phi = 0.3$, corresponding to a density $\bar{\rho} \approx 0.38$. Particles are self-propelled with speed $v_0 = 80$, which results in a drive amplitude of $\Delta\mu \approx 2.2$, by setting $\lambda = 10^{-3}$ and $k_{\mathrm{eff}}\lambda = 50$. Note that we employ dimensionless quantities by reporting all numerical values of lengths in units of σ, energies in units of $k_{\mathrm{B}}T$, and times in units of σ^2/D_0. The rotational diffusion coefficient is set to $D_{\mathrm{r}} = 3$. Assuming particles to be hard Brownian disks, we integrate their equations of motion

$$\dot{\mathbf{r}}_i = v_0\mathbf{e}_i - \mu_0\nabla_i U + \sqrt{2D_0}\boldsymbol{\xi}_i, \qquad \dot{\varphi}_i = \sqrt{2D_{\mathrm{r}}}\xi_i^{\mathrm{r}} \tag{F4}$$

with time step $\delta t = 5 \times 10^{-6}$. Here, components of $\boldsymbol{\xi}_i$ and ξ_i^{r} are drawn from a uniform distribution over $[-\sqrt{3}, \sqrt{3}]$. We model excluded volume via the repulsive short-ranged Weeks-Chandler-Anderson potential $u(r; \epsilon_0, \sigma)$ [see Eq. (F1)], with potential energy well given by $\epsilon_0 = 100$ and r the distance between colloidal particles. The potential is $U = \sum_{i<j} u(|\mathbf{r}_i - \mathbf{r}_j|)$.

The data presented in Figs. 6(b)–6(d) are obtained by dividing the simulation box into equally sized bins and calculating concerned averages within each such bin. To improve statistics, discrete binned data are time averaged over several snapshots with sampling frequency $\tau' = 0.5$ and in batches for the correlation function. Spatial derivatives entering the dissipation rate [see Eq. (41)] are calculated by employing a central difference scheme, respecting periodic boundary conditions, on the discretized data.

[1] I. Müller, *A History of Thermodynamics* (Springer, Berlin, 2007).

[2] J. Schnakenberg, *Network theory of microscopic and macroscopic behavior of master equation systems*, Rev. Mod. Phys. **48**, 571 (1976).

[3] P. Gaspard, *Time-reversed dynamical entropy and irreversibility in Markovian random processes*, J. Stat. Phys. **117**, 599 (2004).

[4] U. Seifert, *Entropy production along a stochastic trajectory and an integral fluctuation theorem*, Phys. Rev. Lett. **95**, 040602 (2005).

[5] J. M. R. Parrondo, C. V. D. Broeck, and R. Kawai, *Entropy production and the arrow of time*, New J. Phys. **11**, 073008 (2009).

[6] G. T. Landi and M. Paternostro, *Irreversible entropy production: From classical to quantum*, Rev. Mod. Phys. **93**, 035008 (2021).

[7] H. Berg and E. Purcell, *Physics of chemoreception*, Biophys. J. **20**, 193 (1977).

[8] F. Rieke and D. A. Baylor, *Single-photon detection by rod cells of the retina*, Rev. Mod. Phys. **70**, 1027 (1998).

[9] S. T. Rutherford and B. L. Bassler, *Bacterial quorum sensing: Its role in virulence and possibilities for its control*, Cold Spring Harbor Perspect. Med. **2**, a012427 (2012).

[10] A. Kornberg and T. A. Baker, *DNA Replication*, 2nd ed. (University Science Books, Sausalito, CA, 2005).

[11] J. L. England, *Statistical physics of self-replication*, J. Chem. Phys. **139**, 121923 (2013).

[12] D. Oriola, D. J. Needleman, and J. Brugués, *The physics of the metaphase spindle*, Annu. Rev. Biophys. **47**, 655 (2018).

[13] G. F. Oster and A. S. Perelson, *The physics of cell motility*, J. Cell Sci. **1987**, 35 (1987).

[14] T. Mitchison and L. Cramer, *Actin-based cell motility and cell locomotion*, Cell **84**, 371 (1996).

[15] U. S. Schwarz and S. A. Safran, *Physics of adherent cells*, Rev. Mod. Phys. **85**, 1327 (2013).

[16] M. C. Marchetti, J. F. Joanny, S. Ramaswamy, T. B. Liverpool, J. Prost, M. Rao, and R. A. Simha, *Hydrodynamics of soft active matter*, Rev. Mod. Phys. **85**, 1143 (2013).

[17] C. Bechinger, R. Di Leonardo, H. Löwen, C. Reichhardt, G. Volpe, and G. Volpe, *Active particles in complex and crowded environments*, Rev. Mod. Phys. **88**, 045006 (2016).

[18] G. Gompper *et al.*, *The 2020 motile active matter roadmap*, J. Phys. Condens. Matter **32**, 193001 (2020).

[19] J. R. Howse, R. A. L. Jones, A. J. Ryan, T. Gough, R. Vafabakhsh, and R. Golestanian, *Self-motile colloidal particles: From directed propulsion to random walk*, Phys. Rev. Lett. **99**, 048102 (2007).

[20] I. Buttinoni, J. Bialké, F. Kümmel, H. Löwen, C. Bechinger, and T. Speck, *Dynamical clustering and phase separation in suspensions of self-propelled colloidal particles*, Phys. Rev. Lett. **110**, 238301 (2013).

[21] H.-R. Jiang, N. Yoshinaga, and M. Sano, *Active motion of a Janus particle by self-thermophoresis in a defocused laser beam*, Phys. Rev. Lett. **105**, 268302 (2010).

[22] J. Palacci, S. Sacanna, A. P. Steinberg, D. J. Pine, and P. M. Chaikin, *Living crystals of light-activated colloidal surfers*, Science **339**, 936 (2013).

[23] H. R. Vutukuri, M. Lisicki, E. Lauga, and J. Vermant, *Light-switchable propulsion of active particles with reversible interactions*, Nat. Commun. **11**, 2628 (2020).

[24] A. Bricard, J.-B. Caussin, N. Desreumaux, O. Dauchot, and D. Bartolo, *Emergence of macroscopic directed motion in populations of motile colloids*, Nature (London) **503**, 95 (2013).

[25] D. Das and E. Lauga, *Active particles powered by Quincke rotation in a bulk fluid*, Phys. Rev. Lett. **122**, 194503 (2019).

[26] J. Yan, M. Han, J. Zhang, C. Xu, E. Luijten, and S. Granick, *Reconfiguring active particles by electrostatic imbalance*, Nat. Mater. **15**, 1095 (2016).
[27] W. Wang, L. A. Castro, M. Hoyos, and T. E. Mallouk, *Autonomous motion of metallic microrods propelled by ultrasound*, ACS Nano **6**, 6122 (2012).
[28] J. L. Anderson, *Colloid transport by interfacial forces*, Annu. Rev. Fluid Mech. **21**, 61 (1989).
[29] R. Golestanian, T. B. Liverpool, and A. Ajdari, *Propulsion of a molecular machine by asymmetric distribution of reaction products*, Phys. Rev. Lett. **94**, 220801 (2005).
[30] R. Golestanian, T. B. Liverpool, and A. Ajdari, *Designing phoretic micro- and nano-swimmers*, New J. Phys. **9**, 126 (2007).
[31] B. Sabass and U. Seifert, *Efficiency of surface-driven motion: Nanoswimmers beat microswimmers*, Phys. Rev. Lett. **105**, 218103 (2010).
[32] B. Sabass and U. Seifert, *Dynamics and efficiency of a self-propelled, diffusiophoretic swimmer*, J. Chem. Phys. **136**, 064508 (2012).
[33] A. S. Khair, *Diffusiophoresis of colloidal particles in neutral solute gradients at finite Péclet number*, J. Fluid Mech. **731**, 64 (2013).
[34] S. Michelin and E. Lauga, *Phoretic self-propulsion at finite Péclet numbers*, J. Fluid Mech. **747**, 572 (2014).
[35] A. Würger, *Self-diffusiophoresis of Janus particles in near-critical mixtures*, Phys. Rev. Lett. **115**, 188304 (2015).
[36] J. De Graaf, G. Rempfer, and C. Holm, *Diffusiophoretic self-propulsion for partially catalytic spherical colloids*, IEEE Trans. Nanobiosci. **14**, 272 (2015).
[37] M. N. Popescu, W. E. Uspal, and S. Dietrich, *Self-diffusiophoresis of chemically active colloids*, Eur. Phys. J. Special Topics **225**, 2189 (2016).
[38] Y. Ibrahim, R. Golestanian, and T. B. Liverpool, *Multiple phoretic mechanisms in the self-propulsion of a Pt-insulator Janus swimmer*, J. Fluid Mech. **828**, 318 (2017).
[39] J. L. Moran and J. D. Posner, *Phoretic self-propulsion*, Annu. Rev. Fluid Mech. **49**, 511 (2017).
[40] M. Lisicki, S. Y. Reigh, and E. Lauga, *Autophoretic motion in three dimensions*, Soft Matter **14**, 3304 (2018).
[41] J. Tailleur and M. E. Cates, *Statistical mechanics of interacting run-and-tumble bacteria*, Phys. Rev. Lett. **100**, 218103 (2008).
[42] Y. Fily and M. C. Marchetti, *Athermal phase separation of self-propelled particles with no alignment*, Phys. Rev. Lett. **108**, 235702 (2012).
[43] G. S. Redner, M. F. Hagan, and A. Baskaran, *Structure and dynamics of a phase-separating active colloidal fluid*, Phys. Rev. Lett. **110**, 055701 (2013).
[44] T. Speck, J. Bialké, A. M. Menzel, and H. Löwen, *Effective Cahn-Hilliard equation for the phase separation of active Brownian particles*, Phys. Rev. Lett. **112**, 218304 (2014).
[45] J. Stenhammar, D. Marenduzzo, R. J. Allen, and M. E. Cates, *Phase behaviour of active Brownian particles: The role of dimensionality*, Soft Matter **10**, 1489 (2014).
[46] M. E. Cates and J. Tailleur, *Motility-induced phase separation*, Annu. Rev. Condens. Matter Phys. **6**, 219 (2015).
[47] G. Liu, A. Patch, F. Bahar, D. Yllanes, R. D. Welch, M. C. Marchetti, S. Thutupalli, and J. W. Shaevitz, *Self-driven phase transitions drive Myxococcus xanthus fruiting body formation*, Phys. Rev. Lett. **122**, 248102 (2019).
[48] J. Toner and Y. Tu, *Flocks, herds, and schools: A quantitative theory of flocking*, Phys. Rev. E **58**, 4828 (1998).
[49] R. Wittkowski, A. Tiribocchi, J. Stenhammar, R. J. Allen, D. Marenduzzo, and M. E. Cates, *Scalar Φ4 field theory for active-particle phase separation*, Nat. Commun. **5**, 4351 (2014).
[50] E. Tjhung, C. Nardini, and M. E. Cates, *Cluster phases and bubbly phase separation in active fluids: Reversal of the Ostwald process*, Phys. Rev. X **8**, 031080 (2018).
[51] D. S. Dean, *Langevin equation for the density of a system of interacting Langevin processes*, J. Phys. A **29**, L613 (1996).
[52] E. Bertin, M. Droz, and G. Grégoire, *Hydrodynamic equations for self-propelled particles: Microscopic derivation and stability analysis*, J. Phys. A **42**, 445001 (2009).
[53] J. Bialké, H. Löwen, and T. Speck, *Microscopic theory for the phase separation of self-propelled repulsive disks*, Europhys. Lett. **103**, 30008 (2013).
[54] T. Speck, *Collective forces in scalar active matter*, Soft Matter **16**, 2652 (2020).
[55] T. Speck, *Critical behavior of active Brownian particles: Connection to field theories*, Phys. Rev. E **105**, 064601 (2022).
[56] G. Pruessner and R. Garcia-Millan, *Field theories of active particle systems and their entropy production*, arXiv:2211.11906.
[57] M. T. Vrugt, J. Bickmann, and R. Wittkowski, *How to derive a predictive field theory for active Brownian particles: A step-by-step tutorial*, J. Phys. Condens. Matter **35**, 313001 (2023).
[58] S. R. de Groot and P. Mazur, *Non-Equilibrium Thermodynamics* (Dover, New York, 1984).
[59] L. Onsager, *Reciprocal relations in irreversible processes. I.*, Phys. Rev. **37**, 405 (1931).
[60] L. Onsager, *Reciprocal relations in irreversible processes. II.*, Phys. Rev. **38**, 2265 (1931).
[61] M. Doi, *Onsager's variational principle in soft matter*, J. Phys. Condens. Matter **23**, 284118 (2011).
[62] P. D. Olmsted and P. Goldbart, *Theory of the nonequilibrium phase transition for nematic liquid crystals under shear flow*, Phys. Rev. A **41**, 4578 (1990).
[63] F. Jülicher, A. Ajdari, and J. Prost, *Modeling molecular motors*, Rev. Mod. Phys. **69**, 1269 (1997).
[64] K. Sekimoto, *Langevin equation and thermodynamics*, Prog. Theor. Phys. Suppl. **130**, 17 (1998).
[65] C. Jarzynski, *Equalities and inequalities: Irreversibility and the second law of thermodynamics at the nanoscale*, Annu. Rev. Condens. Matter Phys. **2**, 329 (2011).
[66] U. Seifert, *Stochastic thermodynamics, fluctuation theorems and molecular machines*, Rep. Prog. Phys. **75**, 126001 (2012).
[67] L. Peliti and S. Pigolotti, *Stochastic Thermodynamics: An Introduction* (Princeton University Press, Princeton, NJ, 2021).

[68] U. Seifert, *Stochastic thermodynamics of single enzymes and molecular motors*, Eur. Phys. J. E **34**, 26 (2011).
[69] T. Schmiedl, T. Speck, and U. Seifert, *Entropy production for mechanically or chemically driven biomolecules*, J. Stat. Phys. **128**, 77 (2007).
[70] T. Speck, *Modeling of biomolecular machines in non-equilibrium steady states*, J. Chem. Phys. **155**, 230901 (2021).
[71] C. Jarzynski, *Nonequilibrium equality for free energy differences*, Phys. Rev. Lett. **78**, 2690 (1997).
[72] C. Jarzynski, *Equilibrium free-energy differences from nonequilibrium measurements: A master-equation approach*, Phys. Rev. E **56**, 5018 (1997).
[73] G. E. Crooks, *Entropy production fluctuation theorem and the nonequilibrium work relation for free energy differences*, Phys. Rev. E **60**, 2721 (1999).
[74] G. E. Crooks, *Path-ensemble averages in systems driven far from equilibrium*, Phys. Rev. E **61**, 2361 (2000).
[75] G. Hummer and A. Szabo, *Free energy reconstruction from nonequilibrium single-molecule pulling experiments*, Proc. Natl. Acad. Sci. U.S.A. **98**, 3658 (2001).
[76] U. Seifert, *From stochastic thermodynamics to thermodynamic inference*, Annu. Rev. Condens. Matter Phys. **10**, 171 (2019).
[77] A. C. Barato and U. Seifert, *Thermodynamic uncertainty relation for biomolecular processes*, Phys. Rev. Lett. **114**, 158101 (2015).
[78] J. M. Horowitz and T. R. Gingrich, *Proof of the finite-time thermodynamic uncertainty relation for steady-state currents*, Phys. Rev. E **96**, 020103(R) (2017).
[79] J. M. Horowitz and T. R. Gingrich, *Thermodynamic uncertainty relations constrain non-equilibrium fluctuations*, Nat. Phys. **16**, 15 (2020).
[80] T. R. Gingrich and J. M. Horowitz, *Fundamental bounds on first passage time fluctuations for currents*, Phys. Rev. Lett. **119**, 170601 (2017).
[81] T. Koyuk and U. Seifert, *Operationally accessible bounds on fluctuations and entropy production in periodically driven systems*, Phys. Rev. Lett. **122**, 230601 (2019).
[82] A. Dechant, *Multidimensional thermodynamic uncertainty relations*, J. Phys. A **52**, 035001 (2019).
[83] T. Koyuk and U. Seifert, *Thermodynamic uncertainty relation for time-dependent driving*, Phys. Rev. Lett. **125**, 260604 (2020).
[84] K. Liu, Z. Gong, and M. Ueda, *Thermodynamic uncertainty relation for arbitrary initial states*, Phys. Rev. Lett. **125**, 140602 (2020).
[85] C. Dieball and A. Godec, *Direct route to thermodynamic uncertainty relations and their saturation*, Phys. Rev. Lett. **130**, 087101 (2023).
[86] D. J. Skinner and J. Dunkel, *Improved bounds on entropy production in living systems*, Proc. Natl. Acad. Sci. U.S.A. **118**, e2024300118 (2021).
[87] J. Van Der Meer, B. Ertel, and U. Seifert, *Thermodynamic inference in partially accessible Markov networks: A unifying perspective from transition-based waiting time distributions*, Phys. Rev. X **12**, 031025 (2022).
[88] P. E. Harunari, A. Dutta, M. Polettini, and É. Roldán, *What to learn from a few visible transitions' statistics?*, Phys. Rev. X **12**, 041026 (2022).
[89] J. Van Der Meer, J. Degünther, and U. Seifert, *Time-resolved statistics of snippets as general framework for model-free entropy estimators*, Phys. Rev. Lett. **130**, 257101 (2023).
[90] P. Pietzonka and F. Coghi, *Thermodynamic cost for precision of general counting observables*, Phys. Rev. E **109**, 064128 (2024).
[91] T. Leonard, B. Lander, U. Seifert, and T. Speck, *Stochastic thermodynamics of fluctuating density fields: Non-equilibrium free energy differences under coarse-graining*, J. Chem. Phys. **139**, 204109 (2013).
[92] D. Forastiere, F. Avanzini, and M. Esposito, *Dissipation in hydrodynamics from micro- to macroscale: Wisdom from Boltzmann and stochastic thermodynamics*, New J. Phys. **26**, 063022 (2024).
[93] G. Falasco and M. Esposito, *Macroscopic stochastic thermodynamics*, Rev. Mod. Phys. **97**, 015002 (2025).
[94] G. Falasco, R. Rao, and M. Esposito, *Information thermodynamics of Turing patterns*, Phys. Rev. Lett. **121**, 108301 (2018).
[95] T. Suchanek, K. Kroy, and S. A. M. Loos, *Entropy production in the nonreciprocal Cahn-Hilliard model*, Phys. Rev. E **108**, 064610 (2023).
[96] T. Suchanek, K. Kroy, and S. A. M. Loos, *Time-reversal and parity-time symmetry breaking in non-Hermitian field theories*, Phys. Rev. E **108**, 064123 (2023).
[97] D. Venturelli, S. A. M. Loos, B. Walter, É. Roldán, and A. Gambassi, *Stochastic thermodynamics of a probe in a fluctuating correlated field*, Europhys. Lett. **146**, 27001 (2024).
[98] T. Speck and R. L. Jack, *Ideal bulk pressure of active Brownian particles*, Phys. Rev. E **93**, 062605 (2016).
[99] É. Fodor, C. Nardini, M. E. Cates, J. Tailleur, P. Visco, and F. van Wijland, *How far from equilibrium is active matter?*, Phys. Rev. Lett. **117**, 038103 (2016).
[100] L. Prawar Dadhichi, A. Maitra, and S. Ramaswamy, *Origins and diagnostics of the nonequilibrium character of active systems*, J. Stat. Mech. (2018) 123201.
[101] F. S. Gnesotto, F. Mura, J. Gladrow, and C. P. Broedersz, *Broken detailed balance and non-equilibrium dynamics in living systems: A review*, Rep. Prog. Phys. **81**, 066601 (2018).
[102] I. A. Martínez, G. Bisker, J. M. Horowitz, and J. M. R. Parrondo, *Inferring broken detailed balance in the absence of observable currents*, Nat. Commun. **10**, 3542 (2019).
[103] G. Szamel, *Stochastic thermodynamics for self-propelled particles*, Phys. Rev. E **100**, 050603(R) (2019).
[104] J. O'Byrne, Y. Kafri, J. Tailleur, and F. Van Wijland, *Time irreversibility in active matter, from micro to macro*, Nat. Rev. Phys. **4**, 167 (2022).
[105] D. Mandal, K. Klymko, and M. R. DeWeese, *Entropy production and fluctuation theorems for active matter*, Phys. Rev. Lett. **119**, 258001 (2017).
[106] C. Nardini, É. Fodor, E. Tjhung, F. van Wijland, J. Tailleur, and M. E. Cates, *Entropy production in field theories without time-reversal symmetry: Quantifying the non-equilibrium character of active matter*, Phys. Rev. X **7**, 021007 (2017).
[107] L. Caprini, U. M. B. Marconi, A. Puglisi, and A. Vulpiani, *Comment on "Entropy production and fluctuation*

theorems for active matter," Phys. Rev. Lett. **121**, 139801 (2018).
[108] S. Shankar and M. C. Marchetti, *Hidden entropy production and work fluctuations in an ideal active gas*, Phys. Rev. E **98**, 020604(R) (2018).
[109] L. Dabelow, S. Bo, and R. Eichhorn, *Irreversibility in active matter systems: Fluctuation theorem and mutual information*, Phys. Rev. X **9**, 021009 (2019).
[110] Ø. L. Borthne, É. Fodor, and M. E. Cates, *Time-reversal symmetry violations and entropy production in field theories of polar active matter*, New J. Phys. **22**, 123012 (2020).
[111] É. Fodor, R. L. Jack, and M. E. Cates, *Irreversibility and biased ensembles in active matter: Insights from stochastic thermodynamics*, Annu. Rev. Condens. Matter Phys. **13**, 215 (2022).
[112] M. J. Bowick, N. Fakhri, M. C. Marchetti, and S. Ramaswamy, *Symmetry, thermodynamics, and topology in active matter*, Phys. Rev. X **12**, 010501 (2022).
[113] T. Agranov, M. E. Cates, and R. L. Jack, *Entropy production and its large deviations in an active lattice gas*, J. Stat. Mech. (2022) 123201.
[114] L. Dabelow and R. Eichhorn, *Thermodynamic nature of irreversibility in active matter*, arXiv:2308.03625.
[115] C. Battle, C. P. Broedersz, N. Fakhri, V. F. Geyer, J. Howard, C. F. Schmidt, and F. C. MacKintosh, *Broken detailed balance at mesoscopic scales in active biological systems*, Science **352**, 604 (2016).
[116] D. S. Seara, V. Yadav, I. Linsmeier, A. P. Tabatabai, P. W. Oakes, S. M. A. Tabei, S. Banerjee, and M. P. Murrell, *Entropy production rate is maximized in non-contractile actomyosin*, Nat. Commun. **9**, 4948 (2018).
[117] S. Ro, B. Guo, A. Shih, T. V. Phan, R. H. Austin, D. Levine, P. M. Chaikin, and S. Martiniani, *Model-free measurement of local entropy production and extractable work in active matter*, Phys. Rev. Lett. **129**, 220601 (2022).
[118] M. E. Cates, É. Fodor, T. Markovich, C. Nardini, and E. Tjhung, *Stochastic hydrodynamics of complex fluids: Discretisation and entropy production*, Entropy **24**, 254 (2022).
[119] T. Nemoto, É. Fodor, M. E. Cates, R. L. Jack, and J. Tailleur, *Optimizing active work: Dynamical phase transitions, collective motion, and jamming*, Phys. Rev. E **99**, 022605 (2019).
[120] É. Fodor, T. Nemoto, and S. Vaikuntanathan, *Dissipation controls transport and phase transitions in active fluids: Mobility, diffusion and biased ensembles*, New J. Phys. **22**, 013052 (2020).
[121] F. Caballero and M. E. Cates, *Stealth entropy production in active field theories near Ising critical points*, Phys. Rev. Lett. **124**, 240604 (2020).
[122] G. Rassolov, L. Tociu, É. Fodor, and S. Vaikuntanathan, *From predicting to learning dissipation from pair correlations of active liquids*, J. Chem. Phys. **157**, 054901 (2022).
[123] F. Ferretti, S. Grosse-Holz, C. Holmes, J. L. Shivers, I. Giardina, T. Mora, and A. M. Walczak, *Signatures of irreversibility in microscopic models of flocking*, Phys. Rev. E **106**, 034608 (2022).
[124] L. K. Davis, K. Proesmans, and É. Fodor, *Active matter under control: Insights from response theory*, Phys. Rev. X **14**, 011012 (2024).
[125] Y. Deng, D. R. Beahm, S. Ionov, and R. Sarpeshkar, *Measuring and modeling energy and power consumption in living microbial cells with a synthetic ATP reporter*, BMC Biol. **19**, 101 (2021).
[126] E. Arunachalam, W. Ireland, X. Yang, and D. Needleman, *Dissecting flux balances to measure energetic costs in cell biology: Techniques and challenges*, Annu. Rev. Condens. Matter Phys. **14**, 211 (2023).
[127] S. Krishnamurthy, S. Ghosh, D. Chatterji, R. Ganapathy, and A. K. Sood, *A micrometre-sized heat engine operating between bacterial reservoirs*, Nat. Phys. **12**, 1134 (2016).
[128] R. Zakine, A. Solon, T. Gingrich, and F. Van Wijland, *Stochastic Stirling engine operating in contact with active baths*, Entropy **19**, 193 (2017).
[129] P. Pietzonka, É. Fodor, C. Lohrmann, M. E. Cates, and U. Seifert, *Autonomous engines driven by active matter: Energetics and design principles*, Phys. Rev. X **9**, 041032 (2019).
[130] V. Holubec, S. Steffenoni, G. Falasco, and K. Kroy, *Active Brownian heat engines*, Phys. Rev. Res. **2**, 043262 (2020).
[131] A. Kumari, P. S. Pal, A. Saha, and S. Lahiri, *Stochastic heat engine using an active particle*, Phys. Rev. E **101**, 032109 (2020).
[132] T. Ekeh, M. E. Cates, and É. Fodor, *Thermodynamic cycles with active matter*, Phys. Rev. E **102**, 010101(R) (2020).
[133] É. Fodor and M. E. Cates, *Active engines: Thermodynamics moves forward*, Europhys. Lett. **134**, 10003 (2021).
[134] P. Malgaretti, P. Nowakowski, and H. Stark, *Mechanical pressure and work cycle of confined active Brownian particles*, Europhys. Lett. **134**, 20002 (2021).
[135] T. Speck, *Efficiency of isothermal active matter engines: Strong driving beats weak driving*, Phys. Rev. E **105**, L012601 (2022).
[136] A. Datta, P. Pietzonka, and A. C. Barato, *Second law for active heat engines*, Phys. Rev. X **12**, 031034 (2022).
[137] P. Gaspard and R. Kapral, *Communication: Mechano-chemical fluctuation theorem and thermodynamics of self-phoretic motors*, J. Chem. Phys. **147**, 211101 (2017).
[138] P. Pietzonka and U. Seifert, *Entropy production of active particles and for particles in active baths*, J. Phys. A **51**, 01LT01 (2018).
[139] T. Speck, *Active Brownian particles driven by constant affinity*, Europhys. Lett. **123**, 20007 (2018).
[140] P. Gaspard and R. Kapral, *Fluctuating chemohydrodynamics and the stochastic motion of self-diffusiophoretic particles*, J. Chem. Phys. **148**, 134104 (2018).
[141] P. Gaspard and R. Kapral, *Thermodynamics and statistical mechanics of chemically powered synthetic nanomotors*, Adv. Phys. X **4**, 1602480 (2019).
[142] J. H. Fritz and U. Seifert, *Thermodynamically consistent model of an active Ornstein-Uhlenbeck particle*, J. Stat. Mech. (2023) 093204.
[143] P. Padmanabha, D. M. Busiello, A. Maritan, and D. Gupta, *Fluctuations of entropy production of a run-and-tumble particle*, Phys. Rev. E **107**, 014129 (2023).
[144] T. Agranov, R. L. Jack, M. E. Cates, and É. Fodor, *Thermodynamically consistent flocking: From discontinuous to continuous transitions*, New J. Phys. **26**, 063006 (2024).
[145] M. Chatzittofi, J. Agudo-Canalejo, and R. Golestanian, *Entropy production and thermodynamic inference for*

stochastic microswimmers, Phys. Rev. Res. **6**, L022044 (2024).
[146] T. Markovich, É. Fodor, E. Tjhung, and M. E. Cates, *Thermodynamics of active field theories: Energetic cost of coupling to reservoirs*, Phys. Rev. X **11**, 021057 (2021).
[147] P. Gaspard and R. Kapral, *Active matter, microreversibility, and thermodynamics*, Research **2020**, 9739231 (2020).
[148] K. Kruse, J. F. Joanny, F. Jülicher, J. Prost, and K. Sekimoto, *Asters, vortices, and rotating spirals in active gels of polar filaments*, Phys. Rev. Lett. **92**, 078101 (2004).
[149] J. Prost, F. Jülicher, and J.-F. Joanny, *Active gel physics*, Nat. Phys. **11**, 111 (2015).
[150] F. Jülicher, S. W. Grill, and G. Salbreux, *Hydrodynamic theory of active matter*, Rep. Prog. Phys. **81**, 076601 (2018).
[151] U. M. Córdova-Figueroa and J. F. Brady, *Osmotic propulsion: The osmotic motor*, Phys. Rev. Lett. **100**, 158303 (2008).
[152] T. Speck, *Thermodynamic approach to the self-diffusiophoresis of colloidal Janus particles*, Phys. Rev. E **99**, 060602(R) (2019).
[153] S. Katz, J. L. Lebowitz, and H. Spohn, *Phase transitions in stationary nonequilibrium states of model lattice systems*, Phys. Rev. B **28**, 1655 (1983).
[154] C. Van Den Broeck and M. Esposito, *Ensemble and trajectory thermodynamics: A brief introduction*, Physica (Amsterdam) **418A**, 6 (2015).
[155] S. Ebbens, M.-H. Tu, J. R. Howse, and R. Golestanian, *Size dependence of the propulsion velocity for catalytic Janus-sphere swimmers*, Phys. Rev. E **85**, 020401(R) (2012).
[156] A. Fischer, A. Chatterjee, and T. Speck, *Aggregation and sedimentation of active Brownian particles at constant affinity*, J. Chem. Phys. **150**, 064910 (2019).
[157] R. L. Stratonovich, *A new representation for stochastic integrals and equations*, SIAM J. Control **4**, 362 (1966).
[158] D. T. Gillespie, *The chemical Langevin equation*, J. Chem. Phys. **113**, 297 (2000).
[159] P. Romanczuk, M. Bär, W. Ebeling, B. Lindner, and L. Schimansky-Geier, *Active Brownian particles: From individual to collective stochastic dynamics*, Eur. Phys. J. Special Topics **202**, 1 (2012).
[160] J. T. Siebert, F. Dittrich, F. Schmid, K. Binder, T. Speck, and P. Virnau, *Critical behavior of active Brownian particles*, Phys. Rev. E **98**, 030601(R) (2018).
[161] P. Digregorio, D. Levis, A. Suma, L. F. Cugliandolo, G. Gonnella, and I. Pagonabarraga, *Full phase diagram of active Brownian disks: From melting to motility-induced phase separation*, Phys. Rev. Lett. **121**, 098003 (2018).
[162] C. Ganguly and D. Chaudhuri, *Stochastic thermodynamics of active Brownian particles*, Phys. Rev. E **88**, 032102 (2013).
[163] I. Di Terlizzi, M. Gironella, D. Herraez-Aguilar, T. Betz, F. Monroy, M. Baiesi, and F. Ritort, *Variance sum rule for entropy production*, Science **383**, 971 (2024).
[164] A. B. Kolomeisky and M. E. Fisher, *Molecular motors: A theorist's perspective*, Annu. Rev. Phys. Chem. **58**, 675 (2007).
[165] E. Zimmermann and U. Seifert, *Efficiencies of a molecular motor: A generic hybrid model applied to the* F_1*-ATPase*, New J. Phys. **14**, 103023 (2012).
[166] F. Khodabandehlou and C. Maes, *Local detailed balance for active particle models*, J. Stat. Mech. (2024) 063205.
[167] D. Saintillan and M. J. Shelley, *Theory of active suspensions*, in *Complex Fluids in Biological Systems*, edited by S. E. Spagnolie (Springer, New York, 2015), pp. 319–355.
[168] J.-P. Hansen and I. R. McDonald, *Theory of Simple Liquids: With Applications of Soft Matter*, fourth ed. (Elsevier/AP, Amsterdam, 2013).
[169] J. H. Irving and J. G. Kirkwood, *The statistical mechanical theory of transport processes. IV. The equations of hydrodynamics*, J. Chem. Phys. **18**, 817 (1950).
[170] J. Bialké, J. T. Siebert, H. Löwen, and T. Speck, *Negative interfacial tension in phase-separated active Brownian particles*, Phys. Rev. Lett. **115**, 098301 (2015).
[171] W. Yan and J. F. Brady, *The force on a boundary in active matter*, J. Fluid Mech. **785**, R1 (2015).
[172] T. Speck, *Stochastic thermodynamics for active matter*, Europhys. Lett. **114**, 30006 (2016).
[173] A. Duzgun and J. V. Selinger, *Active Brownian particles near straight or curved walls: Pressure and boundary layers*, Phys. Rev. E **97**, 032606 (2018).
[174] J. U. Klamser, S. C. Kapfer, and W. Krauth, *Thermodynamic phases in two-dimensional active matter*, Nat. Commun. **9**, 5045 (2018).
[175] M. E. Cates and J. Tailleur, *When are active Brownian particles and run-and-tumble particles equivalent? Consequences for motility-induced phase separation*, Europhys. Lett. **101**, 20010 (2013).
[176] P. C. Hohenberg and B. I. Halperin, *Theory of dynamic critical phenomena*, Rev. Mod. Phys. **49**, 435 (1977).
[177] E. Kalz, A. Sharma, and R. Metzler, *Field theory of active chiral hard disks: A first-principles approach to steric interactions*, J. Phys. A **57**, 265002 (2024).
[178] H. C. Berg and D. A. Brown, *Chemotaxis in Escherichia coli analysed by three-dimensional tracking*, Nature (London) **239**, 500 (1972).
[179] *E. Coli in Motion*, edited by H. C. Berg, Biological and Medical Physics, Biomedical Engineering (Springer, New York, 2004).
[180] D. Needleman and Z. Dogic, *Active matter at the interface between materials science and cell biology*, Nat. Rev. Mater. **2**, 1 (2017).
[181] D. J. Skinner and J. Dunkel, *Estimating entropy production from waiting time distributions*, Phys. Rev. Lett. **127**, 198101 (2021).
[182] A. Daddi-Moussa-Ider, R. Golestanian, and A. Vilfan, *Minimum entropy production by microswimmers with internal dissipation*, Nat. Commun. **14**, 6060 (2023).
[183] A. Dechant, J. Garnier-Brun, and S.-i. Sasa, *Thermodynamic bounds on correlation times*, Phys. Rev. Lett. **131**, 167101 (2023).
[184] S. Hermann and M. Schmidt, *Active ideal sedimentation: Exact two-dimensional steady states*, Soft Matter **14**, 1614 (2018).